

REPORT DOCUMENTATION PAGE

Form Approved
OMB No. 0704-0188

Submit report no longer than the length of a standard 48-line order response, including the time for reviewing instructions, searching existing data sources, gathering and maintaining the data needed, and completing and reviewing the information. Send comments regarding this burden estimate to the Office of the Director of Information Operations and Reports, 1215 Jefferson Davis Highway, Suite 1204, Arlington, VA 22202-4102, and the Defense Management and Audit Paperwork Reduction Project (0704-0188), Washington, D.C. 20303.

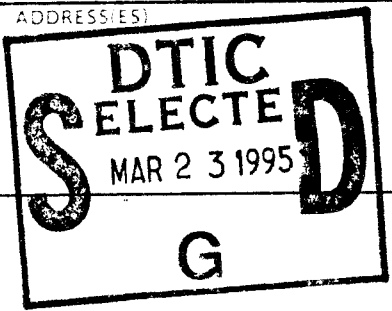
1. AGENCY USE ONLY (Leave blank)	2. REPORT DATE	3. REPORT TYPE AND DATES COVERED FINAL
----------------------------------	----------------	---

4. TITLE AND SUBTITLE Laboratory for Elementary Particle Science	5. FUNDING NUMBERS 61102F
---	------------------------------

6. AUTHOR(S) Gerald A. Smith	2301/DS
---------------------------------	---------

7. PERFORMING ORGANIZATION NAME(S) AND ADDRESS(ES) Penn State University	8. PERFORMING ORGANIZATION REPORT NUMBER AFOSR-TR- 95 0114
---	---

9. SPONSORING/MONITORING AGENCY NAME(S) AND ADDRESS(ES) AFOSR/NE 110 Duncan Avenue Suite B115 Bolling AFB DC 20332-0001	10. SPONSORING/MONITORING AGENCY REPORT NUMBER F49620-92-J-0374
--	--

11. SUPPLEMENTARY NOTES	 DTIC SELECTED MAR 23 1995 G
-------------------------	---

12. DISTRIBUTION AVAILABILITY CODES	13. DISTRIBUTION AVAILABILITY CODES
-------------------------------------	-------------------------------------

APPROVED FOR PUBLIC RELEASE: DISTRIBUTION UNLIMITED

14. SUBJECT TERMS	15. NUMBER OF PAGES			
16. PRICE CODE				
17. SECURITY CLASSIFICATION OF REPORT UNCLASSIFIED		18. SECURITY CLASSIFICATION OF ABSTRACT UNCLASSIFIED	19. SECURITY CLASSIFICATION OF ABSTRACT UNCLASSIFIED	20. LIMITATION OF ABSTRACT UNCLASSIFIED
A-1				

Accession For		
NTIS	CRA&I	<input checked="" type="checkbox"/>
DTIC	TAB	<input type="checkbox"/>
Unannounced		<input type="checkbox"/>
Justification		
By _____		
Distribution /		
Availability Codes		
Dist	Avail and / or Special	
A-1		

17. SECURITY CLASSIFICATION OF REPORT UNCLASSIFIED	18. SECURITY CLASSIFICATION OF ABSTRACT UNCLASSIFIED	19. SECURITY CLASSIFICATION OF ABSTRACT UNCLASSIFIED	20. LIMITATION OF ABSTRACT UNCLASSIFIED
---	---	---	--

10. NUMBER OF PAGES
11. PRICE CODE

12. SECURITY CLASSIFICATION OF ABSTRACT
13. NUMBER OF PAGES
14. PRICE CODE

PENNSTATE



DEPARTMENT OF PHYSICS

PSU LEPS 94/15

AFOSR-TR- 95 0114

FINAL TECHNICAL REPORT

AFOSR GRANT F49620-92-J-0374

June 15, 1992-June 14, 1994

Gerald A. Smith

July 18, 1994

LABORATORY FOR ELEMENTARY
PARTICLE SCIENCE

19950322 127

303 OSMOND LABORATORY

UNIVERSITY PARK, PA 16802

Date: July 18, 1994

To: Dr. Ralph Kelley (AFOSR)

From: Gerald A. Smith, Principal Investigator
AFOSR F49620-92-J-0374

Re: Final Technical Report, June 15, 1992-June 14, 1994

SUMMARY

A detailed report on the results of the first year of funding under this grant was submitted to AFOSR on July 14, 1993. Acknowledgement of technical acceptability of this report was returned on August 24, 1993. The present report is an update on activities for the second year of funding.

Research leading to a detailed characterization of antiproton annihilation in nuclei has resulted in a published analysis of fast deuteron production from carbon and uranium targets. This follows previously reported work and publications by our group on gamma-ray, neutral and charged pion, proton, and neutron production. The deuteron measurements are important to our SHIVA Star antiproton-catalyzed microfission experiment at the Phillips Laboratory, Kirtland AFB, in that they help constrain theoretical models of light nuclei production and subsequent energy deposition in the target.

Work continues at SHIVA Star on working fluid formation and target compression for the microfission experiment. Excellent progress has been made, both theoretically and experimentally, on these important aspects of the experiment.

The Penn State group, working in collaboration with Los Alamos National Laboratory physicists, trapped and held up to 721,000 antiprotons per beam injection pulse from the LEAR accelerator during July, 1993. This was a crucial step to the ultimate goal of transferring large numbers of antiprotons to the Phillips Laboratory for the antiproton-catalyzed microfission experiment.

RESEARCH OBJECTIVES

The objective of this research is to accurately characterize the yields and energy spectra of charged and neutral elementary particles emitted from antiproton annihilation at rest in nuclei (carbon, bismuth and uranium), and to develop design objectives for the subcritical antiproton-catalyzed microfission experiment to be carried out at the Phillips Laboratory, Kirtland AFB, NM.

RESULTS OF RESEARCH

(1) LIGHT NUCLEI EMISSION: During the last year we have completed our efforts on identifying from existing data (LEAR experiment PS183) light nuclei, and have a good signal for deuterons produced

in carbon and uranium. We formed a collaboration with theoretical Russian physicist Dr. Alexander Sibirtsev of the Institute of Theoretical and Experimental Physics, Moscow. This followed naturally after he published a significant analysis of our previously published proton data (A. Sibirtsev, Z.Phys.A 345, 59, 1993). A paper prepared by Dr. Sibirtsev and ourselves (Appendix I) has been published recently. The importance of this work is that it provides, along with the earlier proton analysis, a theoretical basis for understanding light nuclei emission, and subsequent energy deposition in the target.

(2) TARGET COMPRESSION AT SHIVA STAR: Recently first results on working fluid formation inside solid liners at SHIVA Star were published by the High Energy Plasma Division, Phillips Laboratory, Kirtland AFB (Appendix II). This is an important first step in development of the antiproton-catalyzed microfission experiment. Although Penn State personnel are not co-authors on this paper, we have followed this work very closely and participated in computer simulations of these effects.

The Penn State analysis of target compression at SHIVA Star, written in collaboration with Drs. Bell, Degnan, Hussey and Mullins of the Phillips Laboratory, is scheduled to appear in the July 15 issue of the Journal of Applied Physics (Appendix III).

An experiment on solid liner implosion without working fluids was carried out last December at SHIVA Star. The results were in excellent agreement with simulations. A Phillips Laboratory/Penn State collaborative paper has recently been submitted to Phys. Rev. Letters (Appendix IV). Further experiments with working fluids are planned for SHIVA Star later this year.

Therefore, we feel we are making excellent progress toward a theoretical and experimental understanding of target compression for the SHIVA Star antiproton-catalyzed microfission experiment.

(3) ANTIPROTON TRAPPING: During July, 1993 the Los Alamos/Penn State team, working on LEAR experiment PS200, trapped up to 720,000 from accelerator pulses from the LEAR machine. The antiprotons were held in the Los Alamos catcher trap, which is capable of holding up to as many as 10 million antiprotons. Further tests of trapping with multiple pulse filling made possible by electron cooling and improved vacuum are currently in progress.

PUBLICATIONS

1. "Fast Deuteron Production from Antiproton Annihilation at Rest on Carbon and Uranium Targets", A.A. Sibirtsev et al, Z.Phys. A 347, 277 (1994).
2. "Target Compression by Working Fluids Driven with Solid Liner Implosions", J. Appl. Phys. (2), 15 July, 1994.

PARTICIPATING PROFESSIONALS

P.R.Chiang, Ph.D. 1991, "The Effects of Velocity-Space Particle Loss in Field-Reversed Configurations".

R.A.Lewis, Ph.D. 1966, "Pion Photoproduction Angular Distributions"

G.A.Smith, Ph.D.,1961, "Proton-Proton Interactions at 2.85 BeV"

COUPLING ACTIVITIES

A) Colloquia, Lectures and Seminars

INVITED PAPER, 5th Annual Symposium, Penn State University Space Engineering Reserch Center, 1993.

INVITED PAPER, 5th Advanced Space Propulsion Workshop, Jet Propulsion Laboratory, Pasadena, California, 1994.

B) Consulting

Los Alamos National Laboratory, consultant contract, Oct. 1, 1991-July 30, 1994; contact Dr. Nicholas King (P-15 Div.).

Phillips Laboratory, Kirtland AFB, NM, IPA contract, Oct.1, 1991-Sept.30, 1993; contact-Dr.James Degnan (High Energy Plasma Div.).

APPENDIX I

Fast deuteron production from antiproton annihilation at rest on carbon and uranium targets

A.A. Sibirtsev¹, T.A. Armstrong², C. Lam^{2*}, R.A. Lewis², E.D. Minor², G.A. Smith²

¹ Institute of Theoretical and Experimental Physics, B. Cheremushkinskaya ul. 25, Moscow, Russia

² Laboratory for Elementary Particle Science, Department of Physics, 303 Osmond Laboratory, Pennsylvania State University, University Park, PA 16802, USA (Tel. +814/863-3076, FAX: +814/863-3297)

Received: 14 October 1993

Abstract. Deuteron yields from 20–350 MeV kinetic energy in antiproton annihilation at rest in ^{12}C and ^{238}U targets are compared with a coalescence model calculation. Agreement of the data with the model up to approximately 80 MeV is good. However, from 80 to 350 MeV the model increasingly underestimates the yield, by as much as an order of magnitude. These results, along with previously reported failures to explain proton spectra with first order rescattering of pions, suggest that other mechanisms are manifest in relatively rare, high energy light nucleus emission, e.g. $B > 0$ annihilations or possible six quark interactions.

PACS: 13.75.Cs

1. Introduction

During the last ten years much effort has been devoted to the experimental search for multinucleon phenomena in antiproton-nucleus annihilations. The possibility of antiproton annihilation on more than one nucleon has been an important topic of discussion ever since it was suggested by Pontecorvo [1] in 1957.

In the framework of the conventional picture, the antiproton annihilates on a single nucleon and produces mesons that are rescattered in the nuclear environment. In this case the baryon number of the annihilating system is equal to zero. However, there also exists the possibility of annihilations that directly involve several nucleons simultaneously ($B > 0$ annihilations). The principal question arises as to how to distinguish between $B > 0$ annihilation and more prosaic forms of the interaction.

Obviously, a reliable signature for multinucleon annihilation is of special interest [2–4]. An attractive $B > 0$

signal involves enhancement of the strange particle yield. Following Rafelski and Hagedorn [2], enhanced production of strange hadrons can also be the signature of the quark-gluon plasma. Cugnon and Vandermeulen [4] calculated the total yield of strange and nonstrange particles in $B > 0$ annihilation and predicted strangeness as a clear signal for multinucleon phenomena. However, a detailed analysis of experimental data on strange particle production confirmed the conventional annihilation picture [5]. It is likely that rescattering of annihilation mesons ($\bar{p} + N \rightarrow M, M + N \rightarrow K, Y$) explains strangeness production without a $B > 0$ mechanism.

Another possible signature for multinucleon phenomena is enhancement of fast nucleon production. Obviously, at low antiproton energies nucleons are not produced directly in $\bar{p}N$ annihilations (in the case of $B = 0$), and we must incorporate conventional rescattering mechanisms ($\bar{p} + N \rightarrow M, M + N \rightarrow N$) in order to explain the data. Because low energy nucleons are produced via deexcitation of the nucleus, we pay special attention to secondary nucleons with kinetic energies above 20 MeV. One component of fast nucleons is produced in the rescattering of annihilation mesons, or the two-step process. We hypothesize that a second component of very high energy nucleons can be produced via antiproton interaction with several bound nucleons, followed by the transfer of annihilation energy to one of the nucleons. Experimental data on proton production in $\bar{p}^{12}\text{C}$ and $\bar{p}^{238}\text{U}$ annihilation at rest show significant yields of fast protons with energy above ~ 600 MeV [6]. Although interpretation of these results by means of the two-step process seems reasonable to the first approximation [7], it was necessary to incorporate a large probability for antiproton absorption on two bound nucleons, or six-quark objects (q^6), inside the nucleus to explain the data in detail [6, 7].

Our previous studies of fast proton production in $\bar{p}^{12}\text{C}$ and $\bar{p}^{238}\text{U}$ annihilation at rest [6, 7] resulted in two essential conclusions. First, because nucleons already exist inside the nucleus, one needs an energetic projectile to knock them out. The only question is how

Work supported in part by the U.S. Air Force Office of Scientific Research and the National Science Foundation

* National Science Foundation Research Experiences for Undergraduates Awardee

to produce such projectiles in $\bar{p}N$ annihilation. Second, a large q^6 admixture was required to fit the fast proton data. The possible existence of such q^6 states is an intriguing problem in its own right.

Consequently, we have turned to the production of fast deuterons in antiproton-nucleus annihilations. The main background to the $B > 0$ and q^6 processes is deuteron formation via the coalescence mechanism [8]. In the conventional picture, we consider the cascade process that involves annihilation pions in rescatterings in order to create neutron-proton pairs. When a pair possesses a wave function which overlaps with the deuteron, these nucleons may coalesce to form a deuteron. As was shown by Lobov and Sibirtsev [9] and Gugelot and Paul [10], high energy pairs have large relative momenta q and thus, because of the q^{-2} dependence of the deuteron form factor, cannot form a deuteron. Thus, we need to involve other production mechanisms.

The deuteron data discussed in this paper above 120 MeV deuteron kinetic energy have been reported previously [11]. A cut of mass > 1580 MeV was made to isolate the deuteron signal. A separate analysis of these data indicated that contamination of particles with the same q/M , e.g. alpha particles, is $< 1\%$. As in the previous study of proton spectra [6], data from another experiment [12] on low-energy deuterons have been used to provide a complete deuteron spectrum above 20 MeV kinetic energy.

2. Coalescence deuterons

Deuteron spectra below ~ 120 MeV from high energy proton-proton, proton-nucleus and heavy ion collisions have been successfully explained by a coalescence model [8–10]. The model assumes that $n-p$ pairs form a deuteron when the $n-p$ wave function overlaps with the deuteron wave function. Sata and Yazaki [8] formulated the coalescence model for composite particle spectra from high energy collisions in terms of a density matrix formalism and the internal wave function of the composite particle. The deuteron production cross section is given by

$$\frac{d^3 \sigma_{p+A \rightarrow d+X}}{d^3 Q} = \sigma_0 \int d^3 q \phi(q) D_{np}(q, Q), \quad (1)$$

where σ_0 is the inelastic cross section for $\bar{p}A$ interactions, $\phi(q)$ is the deuteron wave function squared, and $D_{np}(q, Q)$ is the $n-p$ two-particle density matrix, with total momentum Q and relative momentum $2p$ for the $n-p$ state. The deuteron wave function is parameterized by Alberi et al. [13] as

$$\phi(q) = \sum_i A_i \exp(-B_i q^2), \quad (2)$$

where $A = \{9.007, 20.035, 9.724, 2.142, -0.184\}$ (GeV/c) $^{-3/2}$ and $B = \{1277.26, 370.595, 88.625, 18.904, 2.494\}$ (GeV/c) $^{-2}$. The two-particle density matrix was calculated using the cascade model COMIC, described

Table 1. Number of deuterons with kinetic energies from 20 to 120 MeV produced per 1000 annihilations

Target	Ref. [12]	Model
^{12}C	96 ± 5	98
^{40}Ca	114 ± 5	131
^{63}Cu	152 ± 17	178
^{92}Mo	188 ± 15	195
^{98}Mo	199 ± 16	208
^{238}U	229 ± 16	245

Table 2. Number of deuterons produced with kinetic energies from 20–350 MeV per 1000 annihilations. The errors for [11] are listed (first) statistical and (second) systematic

Target	Kinetic energy (MeV)	Ref. [12]	Ref. [11]	Model
^{12}C	20–120	96 ± 5		98
	120–350		$11 \pm 1 \pm 2$	3
^{238}U	20–120		229 ± 16	245
	120–350		$15 \pm 1 \pm 2$	8

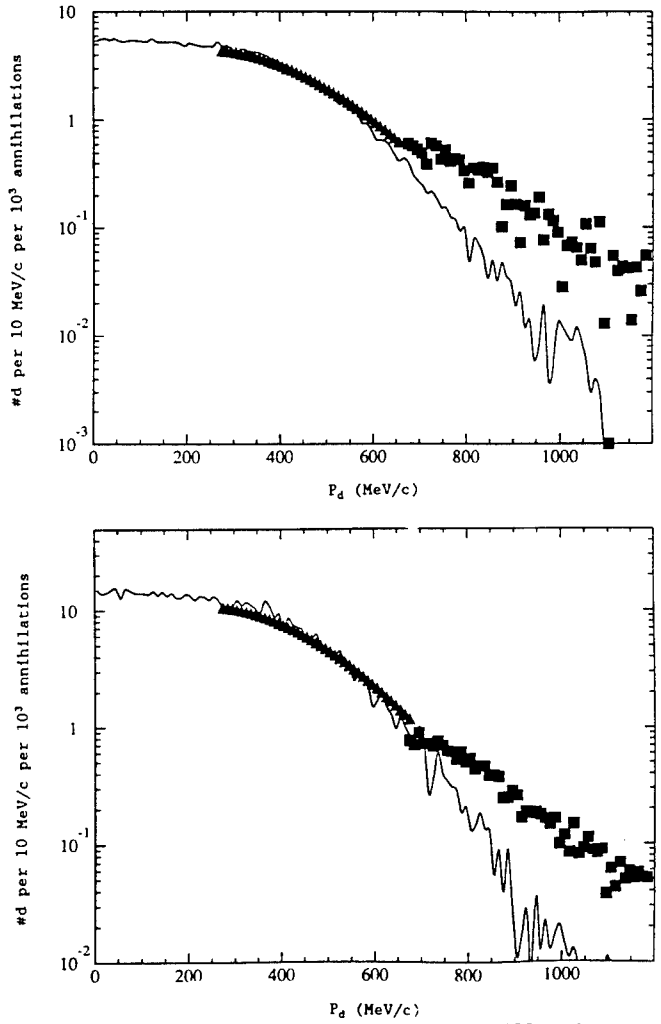


Fig. 1. Number of deuterons per 10 MeV/c per 1000 antiprotons versus deuteron momentum for a ^{12}C and b ^{238}U . The solid squares are data, the line coalescence model predictions. The scatter of data and model predictions above ~ 600 MeV/c is statistical

in detail in [14]. We assume antiproton annihilation on a single nucleon, followed by rescattering of the produced pions in the nuclear environment.

In Table 1 yields of deuterons with kinetic energies from 20 to 120 MeV produced in antiproton annihilation on various nuclei [12] are compared with model calculations. In Table 2 we show deuteron yields up to 350 MeV for $\bar{p}^{12}\text{C}$ and $\bar{p}^{238}\text{U}$ annihilation. Yields are studied for two deuteron energy regions in order to compare the experimental data of Hofmann et al. [12], and present results [11], with model predictions.

The low energy deuterons are quite reasonably reproduced by the calculations based on the conventional annihilation picture and the coalescence model. However, high energy deuterons are underestimated by the model by a factor of $\sim 2\text{--}10$. The deuteron momentum spectra are shown in Fig. 1. Noticeably the high momentum ($\gtrsim 550$ MeV/c, or 80 MeV kinetic energy) component of the deuteron spectra is not well reproduced by the model calculations.

3. Conclusions

We have attempted to explain high energy deuteron production by antiproton annihilation at rest in ^{12}C and ^{238}U targets in terms of a coalescence model. We find that yields below about 80 MeV are in agreement with the coalescence model. However, yields above 80 MeV increasingly are underestimated by the model, by a factor of $\sim 2\text{--}10$ averaged over target and deuteron energy.

At the highest energy (350 MeV), the discrepancy is over one order of magnitude.

As in the case of proton production [6, 7], it appears that models based on first order rescattering do not explain the high energy part of the deuteron spectrum. This suggests that other phenomena, e.g. $B > 0$ interactions, are manifest in the relatively rare high energy part of the spectra of protons and deuterons.

References

1. Pontecorvo, B.M.: JETP **3**, 966 (1957)
2. Rafelski, J., Hagedorn, R.: Thermodynamics of quarks and hadrons. Satz, H. (ed.). Amsterdam: North Holland 1981
3. Kahana, S.: Proceedings of the Workshop on Physics at LEAR. Gastaldi, U., Klapisch, R. (eds.). New York: Plenum Press 1984
4. Cugnon, J., Vandermeulen, J.: Phys. Rev. C **39**, 181 (1989)
5. Cugnon, J., Lombard, R.M.: Nucl. Phys. A **422**, 635 (1984)
6. Minor, E.D., Armstrong, T.A., Chen, B., Lewis, R.A., Smith, G.A.: Z. Phys. A **342**, 447 (1992)
7. Sibirtsev, A.A.: Z. Phys. A **345**, 59 (1993)
8. Sato, H., Yazaki, K.: Phys. Lett. **98B**, 153 (1981)
9. Lobov, G.A., Sibirtsev, A.A.: Sov. J. Nucl. Phys. **52**, 1077 (1990)
10. Gugelot, P.C., Paul, S.M.: Z. Phys. A **344**, 325 (1993)
11. Minor, E.D., Armstrong, T.A., Bishop, R., Harris, V., Lewis, R.A., Smith, G.A.: Z. Phys. A **336**, 461 (1990)
12. Hofmann, P., Hartmann, F.J., Daniel, H., Von Egidy, T., Kanert, W., Markiel, W., Plendl, H.S., Machner, H., Riepe, G., Protic, D., Ziock, K., Marshall, R., Reidy, J.J.: Nucl. Phys. A **512**, 669 (1990)
13. Alberi, G., Rosa, L.P., Thomé, Z.D.: Phys. Rev. Lett. **34**, 503 (1975)
14. Sibirtsev, A.A.: Sov. J. Nucl. Phys. **55**, 541 (1992)

APPENDIX II

Formation of plasma working fluids for compression by liner implosions

F. M. Lehr, A. Alaniz,^{a)} J. D. Beason,^{b)} L. C. Carswell,^{c)} J. H. Degnan, J. F. Crawford,^{d)} S. E. Englert, T. J. Englert, J. M. Gahl,^{e)} J. H. Holmes, T. W. Hussey, G. F. Kiutu, B. W. Mullins,^{f)} R. E. Peterkin, Jr., N. F. Roderick,^{g)} and P. J. Turchi^{h)}
High Energy Plasma Division, Phillips Laboratory, Kirtland Air Force Base, New Mexico 87117-5776

J. D. Graham
Maxwell Laboratories, Inc., Albuquerque, New Mexico 87119

(Received 9 June 1993; accepted for publication 14 December 1993)

Research on the formation of a hot hydrogen working fluid, which may be used in multiple concentric solid-density liner implosions, is reported. In such implosions, an axisymmetric outer liner is driven by a multi-megamp axial discharge, and a coaxial inner liner is driven by a working fluid contained between the liners. The fluid is shocklessly compressed to high pressure as the outer liner implodes around it. In the work reported here a 10 to 100 Torr pressure, hydrogen filled coaxial gun discharge was used to inject plasma into a diagnostic chamber simulating an interliner volume. Spectroscopically determined electron densities of between 10^{17} and 10^{18} cm⁻³ and electron temperatures in the 0.5–2.0 eV range were obtained with a fair degree of reproducibility and symmetry. Two-dimensional, time-dependent magnetohydrodynamic computer simulations of the working fluid formation experiment have been performed, and the computations suggest that the present experiment achieves electron number densities and temperatures at the lower extreme of these limits, and neutral densities $\sim 0.3\text{--}1.0 \times 10^{19}$ cm⁻³. The simulations further suggest that the upper range, and beyond, can be achieved in a more energetic version of the present experiment.

I. INTRODUCTION

Electromagnetically imploded solid liners have been employed at a number of laboratories throughout the world as a means of achieving high energy density for a variety of applications.^{1–6} These solid liners are essentially solid Z pinches⁷ in which the mass of the shell imploded by $J \times B$ forces is sufficiently high that Joule heating during the run-in phase of the implosion is insufficient to cause vaporization. Such devices have achieved depth average implosion velocities of approximately 10 km/s, with inner surface velocities that are a factor of two higher.⁵ Chernyshev⁸ has recently proposed that such liners can be used to compress magnetic flux that is interior to the inner surface of the liner to sufficiently high density that the field can, in turn, implode a central target or liner. This magnetic “working fluid” decouples outer implosion non-uniformities from the central implosion and offers the possibility of coupling non-spherical liner implosion energy onto a spherical compression target. A possible drawback

to such a system is related to the divergence-free, vector nature of the magnetic field and to the intrinsic cylindrical symmetry of the system.

At the Phillips Laboratory we are exploring the possibility of using hot hydrogen as the working fluid in place of the magnetic field. This concept is shown schematically in Fig. 1. Such an arrangement avoids the intrinsic symmetry problem of the fields but introduces a whole new set of difficulties associated with shock waves and pressure uniformity in the hydrogen. For the Phillips Laboratory working fluid scheme, the exclusion of as much magnetic flux from the payload volume as possible is important if spherical symmetry of the implosion is to be achieved. A mixture of plasma and flux would result in a combination of cylindrical and spherical symmetry in the liner implosion. Cylindrical compression is at best two-dimensional, whereas spherical symmetry would result in a three-dimensional compression. A predominantly spherical implosion is superior to a cylindrical one because the former enhances the volume compression ratio.

A relatively uniform pressure distribution in the working fluid as it is compressed by a liner is preferred. Avoiding shock formation during compression makes it easier to keep the distribution uniform, and may be achieved by having the fluid sound speed greater than the inner surface implosion velocity of the outer liner. Uniform, shockless compression of the fluid also suggests applications other than spherical implosions, such as high pressure equation of state studies or hypervelocity projectile acceleration. While the peak liner implosion velocity might reach 10–20 km/s, this is achieved only at late times after the hydrogen has been significantly compressed.

^{a)}Present address: Dept. of Physics, The University of Texas at Austin, Austin, TX 78713.

^{b)}Present address: Dept. of Physics, Headquarters USAFA, U.S. Air Force Academy, CO 80840.

^{c)}Present address: TPS/EDB, Edwards Air Force Base, CA 93523.

^{d)}Present address: Maxwell Laboratories, Inc., San Diego, CA 92123.

^{e)}Permanent address: Dept. of Electrical and Computer Engineering, The University of New Mexico, Albuquerque, NM 87131.

^{f)}Present address: SAF/AQ, The Pentagon, Washington, DC 20330.

^{g)}Permanent address: Dept. of Chemical and Nuclear Engineering, The University of New Mexico, Albuquerque, NM 87131.

^{h)}Permanent address: Dept. of Aeronautical and Astronautical Engineering, The Ohio State University, Columbus, OH 43210.

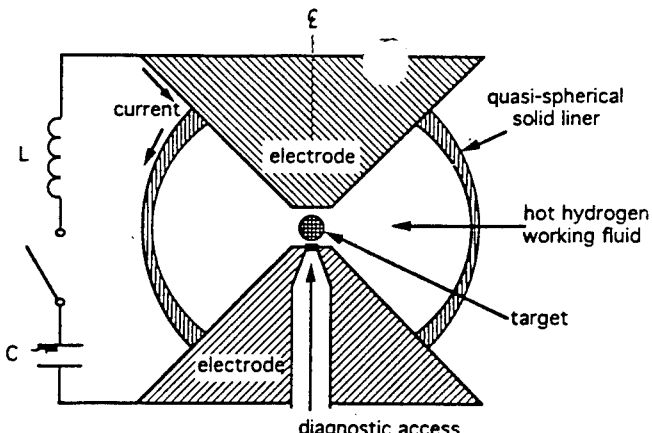


FIG. 1. Schematic of the solid liner implosion concept. Note that the liner is thinner at the equator than it is nearer the poles, accounting for the fact that magnetic pressure varies as $1/r^2$, where r is the radius in cylindrical geometry.

Calculations suggest that an initial temperature in the range of 1 eV is sufficient to assure isotropy, and wall heating considerations dictate that the lowest possible temperature should be used. Knowing the initial temperature, an estimate of the required initial density from the desired final pressure can be made. A factor of ten to twenty radial convergence is routinely obtained from cylindrical plasma Z-pinch implosions, while significantly greater convergence has proven difficult to achieve.⁹ If similar limitations are assumed to apply to solid liners, and if a quasi-spherical implosion is produced as shown in Fig. 1, it appears that the working fluid can be compressed by a factor of 1000 to 8000 in density.

Because of various energy loss mechanisms, including radiative losses and phase transitions such as molecular dissociation and atomic ionization, the working fluid pressure will not increase like that of a $\gamma=5/3$ ideal gas. Instead, it has been determined from two-dimensional CALE calculations¹⁰ that these non-ideal processes may be accounted for by using an effective γ of 1.2–1.4.¹¹ If the ultimate goal is to reach a pressure in excess of 10 Mbar, an initial pressure of 30–600 bar (depending on the assumed radial compression and assuming $\gamma=1.4$) is desired in the interliner volume. Such initial pressures can be achieved in a 1 eV plasma of heavy particle number density in the range of 1.0×10^{19} – 2.0×10^{20} cm^{−3}, for implosions with no central liner.¹⁰ This initial pressure requirement is eased somewhat when a central liner is employed, because the fluid volume compression ratio is larger for the same diameter compression ratio.

The purpose of this program, then, is to determine how a uniform, 1 eV, 1.0×10^{19} – 2.0×10^{20} atom/cm³ working fluid can be produced. Experimental and computational efforts to that end are reported in this paper.

II. EXPERIMENTAL APPROACH AND DIAGNOSTICS

The experimental effort, which began in July 1990, used an inverse Z-pinch discharge in a coaxial gun to heat and compress a plasma and to inject it into a “payload

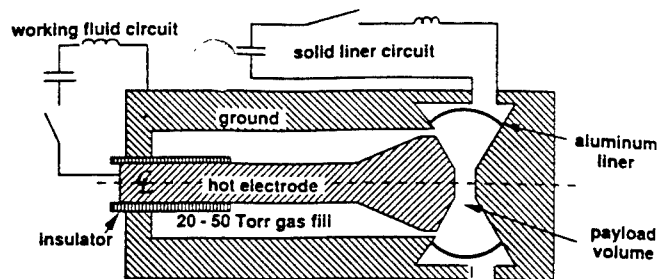


FIG. 2. Schematic of the inverse Z-pinch/coaxial gun working fluid device. Note that the breakdown occurs initially across the insulator, initiating an inverse pinch that heats and partially ionizes the hydrogen. The magnetic force from the discharge then pushes the gas to the right, down the barrel of the coaxial gun, into the payload volume. Even though there was no solid liner present in these experiments, we have indicated where such a liner would be placed.

region” which simulated an interliner volume. Such a device is shown schematically in Fig. 2, which shows how the working fluid injection system would mate with the solid liner. Figure 3 shows an engineering drawing of the actual experimental chamber. The chamber was typically pre-filled with hydrogen to a pressure of between 10 and 100 Torr. Other gases, including deuterium and helium, were also used. In this paper, only those results with hydrogen are discussed. A $44.4 \mu\text{F}$ capacitor bank, storing 35.5 kJ at 40 kV, delivered up to 500 kA to the coaxial gun. The inverse Z-pinch discharge was initiated along a cylindrical pyrex insulator, which was concentric with the gun inner electrode and axially located at the current feed point (see Fig. 2). The current sheath produced by this discharge was driven down the length of the coaxial gun, thus sweeping the prefill gas into the payload volume. The array of rods that surround the insulator and define the outer boundary of the gun allowed the current sheath to expand without excessive shock to the insulator, greatly increasing the insulator life. The chamber was designed to facilitate electrically “floating” the outer conductor and to allow the installation of magnetic flux exclusion inserts in the annular nozzle downstream from the insulator. The experiments

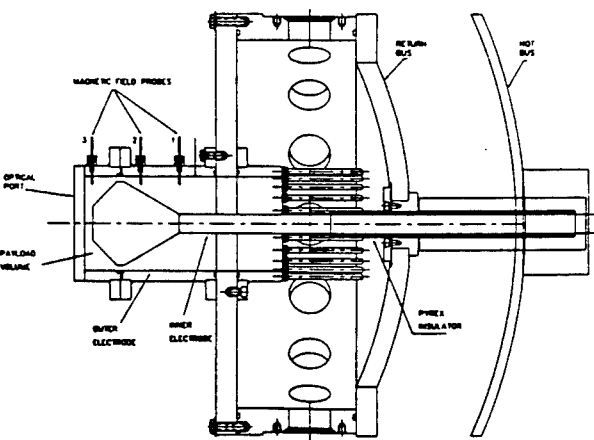


FIG. 3. Diagram of the experimental chamber using the open annular nozzle geometry.

have successfully injected substantial plasma into the payload volume with an outer conductor that was initially either floating or grounded.

In the gun geometry described above, some magnetic flux from the gun discharge was pushed through the annular nozzle into the payload volume. As explained in the introduction, such flux could have deleterious effects on a spherical implosion. It is possible to exclude flux from the payload volume by inserting flux-excluding axial vanes in the annular nozzle. Operation with magnetic flux exclusion inserts will be the topic of a future paper.

An optical multichannel analyzer (OMA) was used to measure the spectral characteristics of the light emitted from the plasma. The optical signals were transmitted through four silica-cored optical fibers of 200 μm diameter. The fibers were oriented to provide chordal views across the payload volume, perpendicular to the axis of the gun. Wavelengths less than 400 nm are sufficiently attenuated in silica that the spectral analysis in this experiment was effectively limited to the visible region. The spectral lines of interest in this range include H_α , H_β , and H_γ at 656.3, 486.1, and 434.0 nm, respectively. The OMA vidicon detector gate pulse was sufficiently short ($\sim 1 \mu\text{s}$) that the spectral sampling represented a small fraction of the plasma time evolution.

Other diagnostics used include magnetic field and voltage probes, and high speed photography using gated microchannel plate (MCP) and rotating mirror fast framing cameras. The MCP camera gate pulse length (i.e., the exposure time) for the results presented in this paper was 200 ns. The microchannel tube gain was set to give appropriate image intensification during this gate time.

III. TIME-DEPENDENT NUMERICAL SIMULATION CODE

To help understand the physics of the working fluid experiment, design experimental hardware, interpret experimental data, and investigate new applications and scaling to different parameter regimes, dynamic computer simulations were performed with MACH2.¹² This code solves the time-dependent, single fluid, multi-temperature, non-ideal radiation magnetohydrodynamic (MHD) equations on a two-dimensional mesh that is composed of arbitrarily shaped quadrilateral cells. A patchwork of logically rectangular collections of cells, which are called blocks, can be made to form an image of the cross section of an axisymmetric experiment; this multiple block structure is ideal for performing numerical simulations of complex experimental configurations such as the coaxial gun and payload volume of this experiment. The code is an arbitrary Lagrangian Eulerian (ALE) code that computes the time-evolution of all three components of the velocity and magnetic vector fields that are fundamental to MHD. Finite differences are computed with a finite volume technique, and a second-order accurate Van Leer convection scheme is used.¹³ Magnetic field advection is accomplished via the flux-conserving constrained transport algorithm of Evans and Hawley¹⁴ that has been generalized to work on non-orthogonal meshes in an ALE code.

For a magnetofluid of mass density, ρ , moving with velocity, \mathbf{u} , in the presence of a magnetic induction, \mathbf{B} , the code solves the fluid momentum equation

$$\rho \frac{D\mathbf{u}}{Dt} = -\nabla P + \mathbf{J} \times \mathbf{B}, \quad (1)$$

the mass continuity equation

$$\frac{D\rho}{Dt} + \rho \nabla \cdot \mathbf{u} = 0, \quad (2)$$

the ion energy equation

$$\frac{D\epsilon_i}{Dt} = -P_i \nabla \cdot \mathbf{u} + \nabla \cdot (\kappa_i \nabla T_i) + \Phi_{ei}, \quad (3)$$

and the electron energy equation

$$\frac{D\epsilon_e}{Dt} = -P_e \nabla \cdot \mathbf{u} + \mathbf{J} \cdot \mathbf{E} + \nabla \cdot (\kappa_e \nabla T_e) - \Phi_{ei} - \Phi_{eR}, \quad (4)$$

where D/Dt represents the usual convective derivative. It is assumed that the atomic occupation numbers can be derived from equilibrium relations of statistical mechanics from the local values of the electron (ion) temperature, $T_{e(i)}$, and the mass density, ρ . It is further assumed that the working fluid is optically thin so that radiation emitted locally by a plasma parcel is not reabsorbed. To check the sensitivity of the results to the thin approximation, additional simulations were performed in which radiative cooling was turned off. Two models for the radiation cooling rate, Φ_{eR} in Eq. (4), have been used. In the standard model,

$$\Phi_{eR} = a_R c \rho \chi_{\text{Planck}} T_e^4 \quad (5)$$

where a_R is Stefan's constant, c is the speed of light, $\rho \chi_{\text{Planck}}$ is the Planck mean opacity for hydrogen, and its inverse, representing an average photon mean free path, is much greater than the linear dimension of the experiment. However, at low temperatures, below $\sim 2 \text{ eV}$, the radiative cooling can be dominated by oxygen impurities that are present in the experiment, and the model of Eq. (5) is insufficient. An alternate model for the radiative cooling rate of hydrogen with a fraction, by number, of oxygen contaminant has been used.^{15,16} The simulations discussed in this paper that include a radiative cooling model used the alternate model with a fractional oxygen impurity of 1 oxygen atom per 10^4 hydrogen atoms.

The dynamical equation for the magnetic field is the magnetic induction equation

$$\frac{\partial \mathbf{B}}{\partial t} = -\nabla \times \mathbf{E}. \quad (6)$$

The electric field, \mathbf{E} , is obtained from a generalized Ohm's law

$$\mathbf{E} = \eta \mathbf{J} - \mathbf{u} \times \mathbf{B} + \frac{\mathbf{J} \times \mathbf{B}}{en_e} - \frac{\nabla P}{2en_e}. \quad (7)$$

The displacement current is assumed to be relatively small so the current density is simply

$$\mathbf{J} = \frac{\nabla \times \mathbf{B}}{\mu_0} \quad (8)$$

This set of equations is closed by equations of state for the electron and ion pressures: $P_{e(i)} = P(\rho, T_{e(i)})$, and by models for the various transport coefficients. The κ are the thermal conductivities of the electrons and the ions. The plasma resistivity, η , is related to the applicable collision frequency: $\eta = m_e v / e^2 n_e$. The electron number density, n_e , depends on the mass density and the mean ionization state, which is computed from the Saha equation and hence is a function of ρ and T_e . In general, the code uses either analytic models or Los Alamos National Laboratory SESAME¹⁷ tables for the equation of state and for thermal conductivities, and for the electrical resistivity. For simulations of the working fluid experiment, classical analytic models were used in which the thermal conductivity is proportional to $T_e^{5/2}$ and in which the electrical resistivity is proportional to $T_e^{-3/2}$. The total pressure, P , is the sum of the ion and electron pressures. Small changes to the temperature are related to small changes to the specific internal energy by a specific heat: $d\varepsilon_{e(i)} = c_{ve(i)} \times (T_{e(i)}) dT_{e(i)}$. Φ_{ei} is an electron-ion coupling term.¹⁸ The code has no model for shear viscosity. The code does include an artificial compressional viscosity, but it is not used in the present simulations.

The simulations of the experiment take place on a two-dimensional mesh of cells that is fixed in the laboratory frame. A time-dependent, self-consistent two-loop RLC circuit model is used to compute the current from the capacitively produced discharge.

Solutions to the dynamic equations (1)–(4) and (6) are strongly influenced by the boundary conditions which are applied to the mass density, the various transport coefficients, the electron and ion specific energies, the components of the magnetic field, and to the components of the velocity. The metallic electrodes are assumed to be perfect electric conductors and modest thermal conductors.

IV. RESULTS

The MCP and fast framing cameras were used to determine whether luminous plasma was injected into the payload volume and to infer the symmetry of the injected plasma from its luminosity. The plasma gun and the payload volume are connected by an annular nozzle. In the experiments reported herein, the annular nozzle was open. Experiments with either a conducting mesh or axial vanes bridging the interelectrode gap were also performed, but are not discussed here. The magnetic field probe signals were used to infer the plasma sheath velocity, the current density within the sheath, and as an additional confirmation of whether the plasma was injected into the payload volume. The MCP photos and the OMA data indicated that, with an open annular nozzle (Fig. 3), substantial plasma injection occurred. For a 50 Torr hydrogen prefill, the initial arrival was azimuthally asymmetric, but the plasma luminosity became more uniform with time. This behavior is illustrated in Fig. 4, where MCP photographs looking along the gun axis show plasma luminosity at 6, 8,

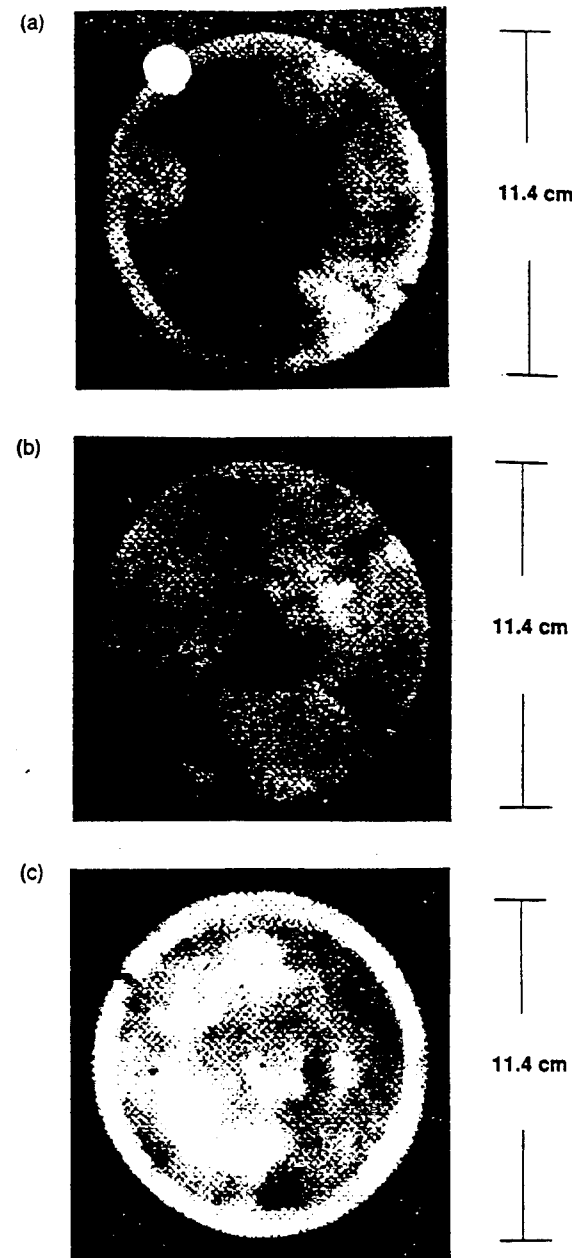


FIG. 4. Microchannel plate camera photos showing the initial azimuthal asymmetry of the plasma as it comes through the annulus. These photographs are for a 40 kV, 44.4 μ F capacitor bank discharge into a 50 Torr hydrogen gas at (a) 6 μ s, (b) 8 μ s, and (c) 18 μ s after current rise.

and 18 μ s after the initiation of the gun discharge. The time of smallest asymmetry, based upon plasma luminosity, typically occurs approximately 15 μ s into the bank discharge.

The causes of azimuthal asymmetry are unclear. One possibility is suggested by studies of discharge initiation versus initial gas fill pressure in the chamber. These studies showed a decrease in the number of current spokes formed during initiation with increasing gas pressure. As the number of spokes decreased, the luminosity of each spoke became more pronounced. The initiation was acceptably uniform at pressures as high as 70 Torr, but at 90 Torr the initiation became too asymmetric to produce the desired condition in the payload volume. It is possible that instabilities introduced during the initiation phase carry over

into the injection phase. This phenomenon requires more study before a definite statement can be made.

Generally, the plasma in the payload volume was sufficiently uniform to permit the electron number density, n_e , and kinetic temperature, T_e , to be obtained from the H_β and H_γ lines in the spectrum. The optical spectra showed a predominantly hydrogen plasma, with occasional silicon lines evident if a glass shielded magnetic field probe was in the OMA fiber field of view, or if the glass insulator broke during a shot. The electron temperature was calculated assuming a plasma in local thermodynamic equilibrium (LTE). For the Balmer series transitions ($n_{\text{lower}}=2$), the requirement for collisional processes to dominate radiative decay and recombination processes is only $n_e > 10^{14} \text{ cm}^{-3}$ (Ref. 19) and was easily satisfied at all times beyond a few μs in this experiment.

The spectra were fitted with Lorentzian functions, and the fitted values were used in the calculations of electron density and temperature. The electron temperature is given by Griem:²⁰

$$kT_e = \frac{E' - E}{\ln(I\lambda^3 g' f' / I'\lambda'^3 g)}, \quad (9)$$

where E' , λ' , and f' are the excitation energy, center wavelength, and oscillator strength, respectively, for the H_γ transition, E , λ , and f , are the corresponding quantities for the H_β transition, and g' and g are the degeneracies for the lower state of each transition. The quantities I and I' are intensities that are obtained from the fitting process. In the present case, the lower state is the same and the degeneracies cancel. Note that Eq. (9) depends only on the relative populations of the two excited states of the species.

Calculation of the electron density can be more difficult, since it is usually necessary to measure absolute intensities. However, in the case of hydrogen, Stark broadening of the H_β line can be used. The electron density is given by²¹

$$n_e = C(n_e, T_e) \Delta\lambda^{3/2}, \quad (10)$$

where $\Delta\lambda$ is the full-width at half-maximum of the peak in the spectrum. The coefficient $C(n_e, T_e)$ is a slowly varying function of both n_e and T_e and is based on Stark profiles for hydrogen. This coefficient is discussed in more detail in Ref. 22.

Optical spectra were obtained in the experiment by viewing the plasma in the payload volume along various chords in the plane whose normal coincided with the axis of symmetry. A representative spectrum is shown in Fig. 5. This spectrum has been fit with Lorentzian functions and the intensities and linewidths obtained from the fits have been used to calculate an electron temperature from Eq. (9) of 0.5–2.0 eV. An electron number density can be obtained from Eq. (10), and the data suggest that $n_e \sim 0.1\text{--}1.0 \times 10^{18} \text{ cm}^{-3}$. The heavy-particle number density can be obtained from the electron number density if the degree of ionization is known. The fractional ionization is quite sensitive to the electron temperature if Saha equilibrium is assumed, and is 10% at 1.2 eV at an ion density of $1.0 \times 10^{19} \text{ cm}^{-3}$. These numbers are typical of the plasmas

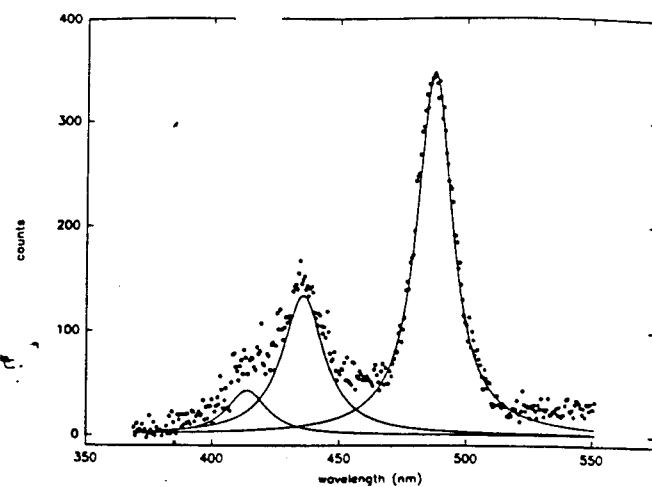


FIG. 5. Optical multichannel analyzer spectrum of a 30 kV, 44.4 μF capacitor discharge into 20 Torr of hydrogen. The spectrum was taken 16 μs into the discharge with a 2 μs window. The spectrum has been corrected for detector response and is fitted with Lorentzian functions.

obtained in the experiments described here. Interpretation of the data, however, is complicated by spatial non-uniformity, and the possibility of resonance absorption. In fact, for some experiments, the H_α line ($n=3$ to $n=2$) at 656.3 nm manifests as a net absorption feature.

The magnetic field was measured with B-dot probes at three axial locations near the outer electrode of the plasma gun as shown in Fig. 3. The B-dot signals were time integrated to yield a signal proportional to the total current flowing between the radial position of the probe and the center conductor. Experimental time histories of the magnetic field at the three probes are compared to the computed discharge current and the simulated magnetic probe signals in Fig. 6. The general shape of the computed signals compares favorably with the experimental data. However, the experimental data do show some azimuthal asymmetry that is not quantified in this figure, and this can account for some of the difference between data and simulations. Approximately 400 kA of the 500 kA discharge current reached the most upstream probe (probe 1) at 5 μs , and the current decayed thereafter on a time scale of approximately 50 μs . The most downstream probe (probe 3) was located in the payload volume. Both the experimental and the simulated current traces indicate that between 100 kA and 150 kA appeared in the payload volume. The magnetic flux associated with this current is undesirable for the reasons stated in the introduction. Based on past experience with flux-excluding vanes,²³ we are confident that the current in the payload volume can be substantially reduced without significant reduction of the fraction of the total mass delivered to that volume.

The time-evolution of the MHD simulation is illustrated in Fig. 7, where isocontours of the heavy particle number density are shown at 4, 8, and 12 μs after the beginning of the discharge. The initial discharge ionizes the hydrogen prefill, and leads to an azimuthal magnetic field of approximately 1 T that drives the hydrogen plasma radially outward during the first 4 μs of the discharge and

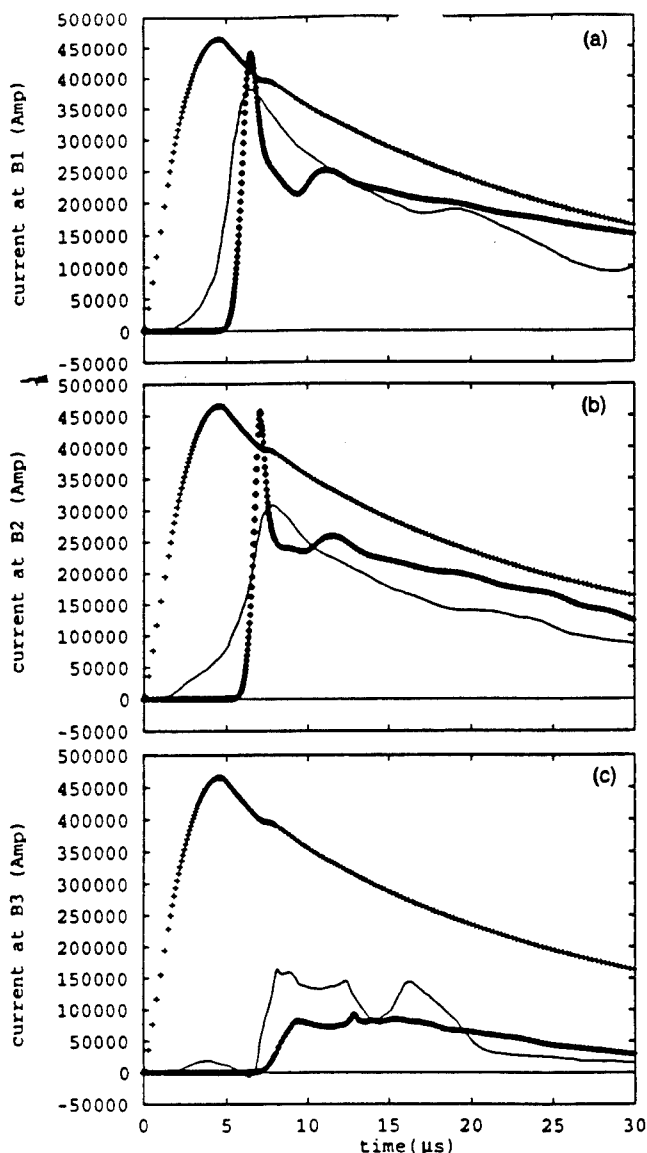


FIG. 6. Comparison between the experimental time-integrated magnetic field probes and the MACH2 simulated current at the three axial probe locations (see Fig. 3). (a) Probe 1, (b) probe 2, and (c) probe 3 for a 40 kV, $44.4 \mu\text{F}$ capacitor bank discharge into 20 Torr of hydrogen. In each frame, the dashed line represents the experimental data, the plus signs represent the capacitor bank current, and the diamonds represent simulated probe data.

axially downstream during the subsequent time of the simulation. The magnetic pressure of the field exceeds the thermal pressure of the plasma and is sufficient to compress the plasma sheath, driving it through the annular nozzle into the payload volume for times greater than 12 μs . The amount of mass that is driven into the payload volume after 15 μs in this simulation is approximately 1.1 mg, which represents 15% of the prefill mass. Some of the mass initially in the gun is driven out through the space between the posts that forms the outer electrode of the gun. The posts are simulated by a flow-through boundary condition in the MHD computations.

The simulation predicts an average heavy particle number density (ions plus neutral atoms) of between 0.3 and $1.0 \times 10^{19} \text{ cm}^{-3}$ at an electron temperature of between

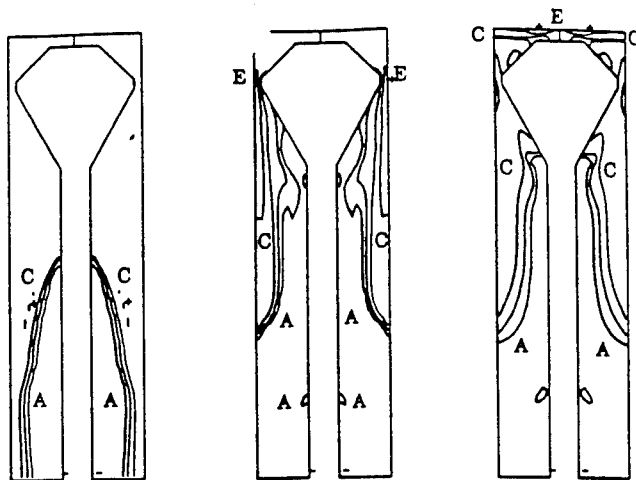


FIG. 7. Isocontours of the heavy particle number density from a MACH2 simulation of the open annular gun geometry with a 40 kV, $44.4 \mu\text{F}$ capacitor bank discharge into 20 Torr of hydrogen. The views are, from left to right, at 4, 8, and 12 μs after the beginning of the gun discharge. The contour levels are logarithmically scaled: A = 1.0×10^{17} , C = 1.0×10^{18} , E = 1.0×10^{19} .

0.35 and 0.75 eV in the payload volume after 20 μs . The higher (lower) density regions are colder (warmer). At these densities, ionization recombination rates are sufficiently large to permit the assumption of Saha ionization equilibrium. The degree of ionization is quite sensitive to temperature, and at an ion density of $1.0 \times 10^{19} \text{ cm}^{-3}$ varies from less than 0.2% at 0.75 eV to full ionization at 3 eV. The degree of ionization of the relatively cool hydrogen plasma is predicted to be <1% in this simulation. This places the simulated electron number density $\sim 1.0 \times 10^{16} \text{ cm}^{-3}$, or at least an order of magnitude below the value suggested by the data if the issue of resonance absorption is ignored. The thermal pressure at the mid-plane of the payload volume is predicted by the simulation to range between 2300–3800 Torr (3–5 bar) in the radial direction at times later than $\sim 15 \mu\text{s}$. It is found that the pressure varies by a factor of 2–3 in the axial direction. These values are well below the 30–600 bar pressure that is desired for a working fluid.

It is important to consider the sensitivity of the electron temperature, and hence the degree of ionization, predicted by the numerical simulation to the models for radiative cooling and for thermal conductivity. It was found that increasing the fraction of oxygen contaminant above the 10^{-4} level that was used in the simulations previously discussed increased the radiative cooling rate and decreased the electron temperature and fractional ionization. At the other extreme, if the radiation cooling model is turned off, the temperature was found to range from 0.4 eV near the axis to 1.0 eV near the outer edge of the payload volume. If, in addition, thermal conduction to the walls is forbidden, the electron temperature falls into the range 0.4–0.9 eV in the payload volume at times beyond 15 μs . At these slightly higher temperatures, the fractional ionization is an order of magnitude higher and brings the simulated electron number density closer to the values

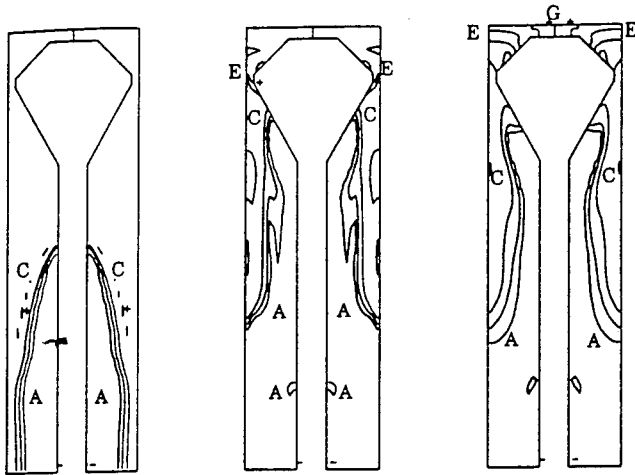


FIG. 8. Isocontours of the heavy particle number density from a MACH2 simulation of the open annular gun geometry with a 40 kV, 88.8 μ F capacitor bank discharge into 20 Torr of hydrogen. The views are, from left to right, at 4, 8, and 12 μ s after the beginning of the gun discharge. The contour levels are logarithmically scaled: $A = 1.0 \times 10^{17}$, $C = 1.0 \times 10^{18}$, $E = 1.0 \times 10^{19}$, $G = 1.0 \times 10^{20}$ cm^{-3} .

measured in the experiment. Although neither radiative cooling nor thermal conduction represent substantial cooling mechanisms at this energy level, they do strongly effect the degree of ionization of the plasma if Saha equilibrium is assumed.

A variety of other potential experimental configurations were investigated with MHD simulations to help obtain a design that yields a greater pressure in the payload volume. Furthermore, a new driver capacitor bank has been constructed that provides up to 125 kJ of stored energy.

The first simulation suggested that increasing the gun energy may increase the fraction of the gas fill that is driven into the payload volume, and may increase the temperature of the plasma. Therefore, a second MACH2 simulation of this plasma gun geometry driven by an 88.8 μ F, 40 kV gun discharge (71 kJ) and a 20 Torr hydrogen prefill was performed. The second simulation predicted a greater mass density in the payload volume after ~ 15 μ s than was obtained in the first. In the later case, the larger magnetic pressure from the more energetic discharge was sufficient to push twice the mass of plasma, or 30% of the total prefill, into the payload volume as the less energetic discharge. In the more energetic case, the average heavy particle density was found to range between 0.3 and 1.0×10^{19} cm^{-3} and the temperature was between 0.6 and 1.0 eV after 20 μ s. This behavior is illustrated in Fig. 8 where isocontours of the heavy particle number density are shown at 4, 8, and 12 μ s after the beginning of the discharge. Comparison between this figure and Fig. 7 shows that the plasma reaches the payload volume somewhat sooner in the more energetic case. Nevertheless, the pressure of the injected hydrogen working fluid was still found to be substantially less than the desired level. Additional simulations with different gun geometries suggest that the

desired pressure may be obtainable with a more energetic discharge in a gun with a larger ratio of gun to payload volume.

V. CONCLUSIONS

The injection of plasma into a ~ 100 cm^3 "payload" diagnostic volume through an open annular nozzle, using ~ 40 kV, ~ 0.5 MA discharges in a 10 to 100 Torr hydrogen filled coaxial gun, was studied. Comparison of MACH2 2- $\frac{1}{2}$ -dimensional MHD simulations with experimental results indicate that a plasma ionized at approximately the 1% level was injected into the payload volume, creating a pressure of between 3 and 5 bar. Direct measurements of the plasma pressure have not yet been made. From data obtained with optical spectroscopy, it was deduced that the temperature was in the 0.5–2.0 eV range. Estimates of the electron number density, made from the measured widths of spectroscopic lines, placed the value in the range between 0.1 and 1.0×10^{18} cm^{-3} . This estimate ignores the possible effect of resonance absorption which may decrease this value somewhat. The measured electron number density was at least an order of magnitude greater than the value predicted by numerical MHD simulations performed with the code MACH2. From experiments, it was estimated that the neutral plus ion number density was $\sim 3.0 \times 10^{18}$ cm^{-3} for a 44.4 μ F, 40 kV gun discharge in a 20 Torr hydrogen prefill. The neutral plus ion number density for higher energy operation was predicted by numerical simulations to be between 3.0×10^{18} and 1.0×10^{19} cm^{-3} . This is close to the range required for the intended applications. At any energy level so far investigated with the MACH2 code, the pressure was found to vary by $\sim 30\%$ in the radial direction, and to vary by a factor of 2–3 in the axial direction at times after the transient portion of the plasma injection process. In addition, there was experimental photographic evidence of azimuthal asymmetry. The ramifications of such pressure variations on solid liner implosions are not yet clear.

The pressure in the payload volume of the present geometry is predicted by MHD simulation, and inferred from spectroscopical measurements, to be substantially less than the 30–600 bar values that are desired for solid liner applications. In future work, superior gun designs will be investigated at higher energy, and direct pressure measurements in the payload volume will be attempted. Techniques to improve pressure uniformity in the payload volume, and the effect of the hot working fluid on an actual implosion liner in the payload volume during injection will be studied. Future work will also explore techniques to exclude magnetic flux from the payload volume.

ACKNOWLEDGMENTS

This work is supported by the Air Force Office of Scientific Research. The authors had many useful discussions with J. Buff of Mission Research Corporation concerning atomic physics issues, and acknowledge his contributions to the development of the low temperature radiation cooling model used in the numerical simulations. The authors

also give special thanks to D. Allap, K. Golby, W. Kaiser, R. Sedillo, and M. Sena of Maxwell Laboratories, Inc., and to G. Baca and M. Dearborn of the Phillips Laboratory for their invaluable technical support on the experiment.

- ¹P. J. Turchi, A. L. Cooper, R. D. Ford, D. J. Jenkins, and R. L. Burton, in *Megagauss Physics and Technology*, edited by P. J. Turchi (Plenum, New York, 1980), p. 375.
- ²S. G. Alikhanov, V. P. Bakhtin, and D. A. Toporkov, *Ultrahigh Magnetic Fields—Physics, Techniques, Applications*, edited by V. M. Titov and G. A. Shvetsov (Nauka, Moscow, 1984), p. 213.
- ³A. G. Eskov, M. I. Kitayev, and R. Kh. Kurtmullayev, in *Ultrahigh Magnetic Fields—Physics, Techniques, Applications*, edited by V. M. Titov and G. A. Shvetsov (Nauka, Moscow, 1984), p. 204.
- ⁴A. A. Petrukhin, N. P. Bidlyo, S. F. Garanin, V. M. Danov, V. V. Zmushko, A. I. Kuzyaev, V. N. Mokhov, E. S. Pavlovskii, V. A. Prokoppov, M. S. Protosov, V. K. Chernyshev, V. A. Shvetsov, and V. B. Yakubov, in *Ultrahigh Magnetic Fields—Physics, Techniques, Applications*, edited by V. M. Titov and G. A. Shvetsov (Nauka, Moscow, 1984), p. 406.
- ⁵J. H. Degnan, M. L. Alme, W. L. Baker, J. S. Buff, C. B. Boyer, C. J. Clouse, S. K. Coffey, D. W. Conley, D. Dietz, J. D. Graham, S. L. Gonzalez, K. E. Hackett, D. J. Hall, J. L. Holmes, E. A. Lopez, W. F. McCullough, D. W. Price, R. E. Reinovsky, N. F. Roderick, P. J. Turchi, and J. M. Welby, in *Megagauss Technology and Pulsed Power Applications*, edited by C. M. Fowler, R. S. Caird, and D. J. Erickson (Plenum, New York, 1987), pp. 699–706.
- ⁶J. H. Degnan, W. L. Baker, J. D. Beason, C. J. Clouse, D. Dietz, D. J. Hall, J. L. Holmes, D. W. Price, and C. R. Sovinec, in *Megagauss Fields and Pulsed Power Systems*, edited by V. M. Titov and G. A. Shvetsov (Nova Science, New York, 1990), pp. 623–630.
- ⁷N. A. Krall and A. W. Trivelpiece, *Principles of Plasma Physics* (McGraw-Hill, New York, 1973).
- ⁸V. K. Chernyshev, V. N. Mokhov, M. S. Protasov, V. B. Yakubov, A. A. Petrukhin, A. I. Kuzyaev, E. S. Pavlovskii, A. M. Buyko, B. E. Grinevitch, V. I. Mamyshev, V. V. Vakhrushev, V. A. Shvetsov, and V. A. Demidov, in *Digest of Technical Papers: Eighth IEEE International Pulsed Power Conference*, 17–19 June 1991, San Diego, CA, edited by R. White and K. Prestwich (The Institute of Electrical and Electronics Engineers, New York, 1991), pp. 438–456.
- ⁹T. W. Hussey, N. F. Roderick, and D. A. Kloc, *J. Appl. Phys.* **51**, 1455 (1980).
- ¹⁰R. E. Tipton, *CALE Users Manual*, Lawrence Livermore National Laboratory, Livermore, CA, 1990.
- ¹¹T. W. Hussey, R. E. Peterkin, D. Dietz, J. H. Degnan, J. D. Beason, N. F. Roderick, and P. J. Turchi, in *IEEE Conference Record—Abstracts 1992 IEEE International Conference on Plasma Science*, June 1–3, 1992, Tampa, FL (The Institute of Electrical and Electronics Engineers, New York, 1992), p. 155.
- ¹²See National Technical Information Service Document No. ADA 192285 (Mission Research Corporation Report AMRC-R-874 by M. H. Frese, 1987). Copies may be obtained from the National Technical Information Service, Springfield, VA 22161. The price is 14.95 plus a 3.00 handling fee. All orders must be prepaid.
- ¹³B. Van Leer, *J. Comp. Phys.* **23**, 276 (1977).
- ¹⁴C. R. Evans and J. F. Hawley, *Astro. Phys. J.* **332**, 659 (1988).
- ¹⁵A. Dalgarno and R. A. McCray, *Ann. Review Astr. Astrophys.* **10**, 375 (1992) (see Table 4).
- ¹⁶S. Wofsey, R. G. H. Reid, and A. Delgarno, *Astrophys. J.* **168**, 161 (1971).
- ¹⁷“SESAME: A Los Alamos National Laboratory Equation of State Data Base,” Los Alamos National Laboratory, Los Alamos, NM, LA-UR-92-3407. The SESAME Equation of State (EOS) Library is a computer based library of tables of thermodynamic properties of a variety of materials. It is maintained by the EOS and Mechanics of Materials Group (T1) of the Theoretical Division of Los Alamos National Laboratory. Address inquiries to SESAME Library, T-1, MS-B221, Los Alamos National Laboratory, Los Alamos, NM 87545.
- ¹⁸S. I. Braginskii, in *Review of Plasma Physics*, edited by M. A. Leontovich (Consultants Bureau, New York, 1965), p. 205.
- ¹⁹R. W. P. McWhirter, in *Plasma Diagnostic Techniques*, edited by R. H. Huddlestane and S. L. Leonard (Academic, New York, 1965), pp. 201–264.
- ²⁰H. Griem, *Plasma Spectroscopy* (McGraw-Hill, New York, 1964), p. 270.
- ²¹*Ibid.*, p. 305.
- ²²*Ibid.*, pp. 538–539.
- ²³J. H. Degnan, W. L. Baker, K. E. Hackett, D. J. Hall, J. L. Holmes, J. B. Kriebel, D. W. Price, R. E. Reinovsky, J. D. Graham, E. A. Lopez, M. L. Alme, G. Bird, C. N. Boyer, S. K. Coffey, D. Conte, J. F. Davis, III, S. W. Seiler, and P. J. Turchi, *IEEE Trans. Plasma. Sci.* **PS-15**, 760 (1987).

APPENDIX III

Target Compression by Working Fluids Driven with Solid Liner Implosions*

P-R. Chiang, R. A. Lewis, and G. A. Smith
Laboratory for Elementary Particle Science, Department of Physics,

J. M. Dailey
Department of Aerospace Engineering,

S. Chakrabarti
Department of Mechanical Engineering

K. I. Higman
Department of Nuclear Engineering

The Pennsylvania State University, University Park, PA 16802

D. Bell, J. H. Degnan, T. W. Hussey and B. W. Mullins

High Energy Plasma Division, Phillips Laboratory, Kirtland AFB, NM 87117

ABSTRACT

Compression by a spherical solid liner of a gold target surrounded by a hydrogen plasma is simulated. Two-dimensional simulations that treat only a subset of the physics included in the one-dimensional code were performed in an attempt to assess multidimensional effects. A one-dimensional numerical code has been developed to study the effects of thermal radiation and conduction. Results of pressure, density and energy deposited for different initial plasma conditions are presented and discussed. Results from both one- and two-dimensional codes show that the average target density at peak compression is 39 - 43 gm/cm³, using the SHIVA Star facility at 90 kV discharge.

* Work supported in part by the Air Force Office of Scientific Research, Jet Propulsion Laboratory (NASA), National Science Foundation, Penn State Propulsion Engineering Research Center Grant NAGW-1356, #8, and the Rocketdyne Corporation.

I. Introduction

Electromagnetically imploded solid liners have been employed at some laboratories as a means of achieving high energy densities and pressures.¹⁻⁷ Solid liner implosions are essentially hollow shell z-pinches⁸ or θ -pinches in which the mass of the liner is sufficient to prevent vaporization of the liner during the run-in phase of the implosion. At the Phillips Laboratory we are planning to use solid liner implosions to compress a hot hydrogen working fluid which will in turn compress an inner target. The advantages of a working fluid include decoupling of outer implosion non-uniformities from the central implosion and the possibility of transferring non-spherical liner energy onto a spherical target.

One application of this technology is antiproton-catalyzed microfission. Antiproton annihilations have been shown to be a strong source of neutrons⁹ and pions¹⁰ which, under conditions of high density, enable a significant reduction in burn time and hence, size of fissile targets. The concept of antiproton-catalyzed microfission¹¹⁻¹² will be tested by compressing a small fissile target with an electromagnetically imploded solid liner. A subcritical test is possible at this time, with presently limited numbers of antiprotons available. To simulate the compression of a solid target, a one-dimensional (1-D) Lagrangian hydrodynamics with radiation code, HYDRAD,¹³ has been developed. A two-dimensional (2-D) magnetohydrodynamics (MHD) code, C-language Arbitrary Lagrangian Eulerian (CALE),¹⁴ is used in order to assess multidimensional effects. Since thermal radiation and conduction are not available in this version of CALE, 1-D calculations with radiation and thermal conduction are performed to study their effects.

The solid liner implosion system is shown schematically in Fig. 1. The quasispherical liner is imploded by a 16 MA peak discharge from the Phillips Laboratory SHIVA Star capacitor bank, which stores 5.3 MJ of energy with 1300 μ F of capacitance at 90 KV. The current which flows through the liner forces it to collapse inward. A tapered spherical aluminum liner (1 mm to 2 mm

thick) encloses 45°-angle conical electrodes and a sealed chamber with a 4-cm radius; a gold target (gold is used instead of uranium due to availability of parametric information, e.g., equation of state, opacity, etc.) and a hydrogen plasma used as a working fluid are placed in the chamber. The implosion is designed to result in an isotropic, adiabatic compression intended to avoid generating shock waves in the target, which lead to undesirable high-temperature, low-density conditions. However, there is a trade-off between the requirement that the working fluid temperature, and hence its sound speed, be high enough so that the plasma will be compressed adiabatically, and the requirement that thermal losses to the walls be minimized. A hydrogen plasma with a temperature between 1-5 eV and density between 10^{19} - 10^{20} cm $^{-3}$ best satisfies these requirements.^{15,16}

In Section II, HYDRAD is described. In Section III, results with different initial plasma parameters, specifically $T_0 = 2$ eV, 5 eV and $n_0 = 1 \times 10^{19}$ cm $^{-3}$, 6×10^{19} cm $^{-3}$, are presented. In Section IV, 1-D results including radiation effects are presented and discussed.

II. Description of HYDRAD and CALE

A. HYDRAD

i) One-Dimensional Hydrodynamics

The model of HYDRAD assumes spherical symmetry and fluid-like solids. The one-dimensional Euler equations in spherical geometry are

$$\frac{\partial v}{\partial t} - \frac{\partial r^2 u}{\partial m} = 0 \quad (\text{continuity}), \quad (1)$$

$$\frac{\partial u}{\partial t} + r^2 \frac{\partial p}{\partial m} = g \quad (\text{momentum}), \quad (2)$$

and

$$\frac{\partial E}{\partial t} + \frac{\partial r^2 u p}{\partial m} = u g - K_{th} + q_{ext} \quad (\text{energy}). \quad (3)$$

Here, $v = 1/p$ is the specific volume, u is the fluid velocity in the radial (r) direction, g is the external force, p is the pressure, E is the internal energy, m is the mass coordinate, K_{th} accounts

for the rate of energy loss due to thermal radiation conduction and q_{ext} is the rate of change of external energy sources.

We use a radiation thermal conduction model¹⁷ to calculate thermal radiation and conduction loss. Thermal conduction due to electrons and ions is included in the calculation by using the following equations, for both plasma and metallic solids:

$$K_{\text{th}} = -\frac{1}{\rho} \nabla \cdot (\kappa \nabla T), \quad (4)$$

$$\kappa = \kappa_i + \kappa_e + \kappa_r, \quad (5)$$

and $\kappa_r = \frac{16\sigma L_R T^3}{3}, \quad (6)$

where T is the temperature, σ is Stefan-Boltzmann constant, L_R is the Rosseland mean free length, and κ_i and κ_e are, respectively, the ion and electron thermal conductivities.

Since a strong shock wave may be created in the solid target due to its initial low temperature, it is necessary to use a sophisticated numerical scheme to account for large pressure and temperature gradients. Therefore, we adopt the piecewise parabolic method (PPM).¹⁸ The PPM scheme is an extension of Godunov's approach,¹⁹ which has; 1) a Riemann solver to handle wave interactions, 2) higher order interpolation techniques, and 3) special monotonicity constraints and discontinuity detectors. The scheme is one of the most accurate numerical methods for hydrodynamics simulations.¹⁹ The accuracy of the method is second order in time and third order in space. Instead of mixing a Lagrangian step and an Eulerian remap step, a pure Lagrangian scheme is used.

The Cranck-Nicholson scheme²⁰ is used for solving the thermal conduction equation and the free stream flux limiter²⁰⁻²² is imposed on thermal conduction coefficients, κ_r and κ_e , to compensate for the diffusion approximation. The numerical model for radiation calculations in HYDRAD is similar to the model of MEDUSA,²² except that HYDRAD uses one temperature only.

ii) Equation-of-State and Rosseland Mean Free Path

To simulate solids, including the target and liner, under compression a three-term model¹⁷ is used to calculate the equation-of-state (EOS), namely,

$$E = E_c(v) + E_i^T(v, T) + E_e^T(v, T), \quad (7)$$

and $P = P_c(v) + P_i^T(v, T) + P_e^T(v, T), \quad (8)$

where $E_c(v)$ and $P_c(v)$ are, respectively, the energy and pressure of the cold isotherms, and subscripts i and e , respectively, indicate the thermal contributions from ions and electrons. Thermal contributions from ions and electrons are expressed in analytical forms.¹⁷ The cold isotherms are generated from the SESAME equation-of-state (EOS) library,²³ and have been fit by a polynomial function to improve computation speed. The advantage of using this three-term model is that the temperature can be analytically computed without interpolation. The EOS model is reasonably accurate up to $T = 20$ eV.

With relatively low initial temperature compared to the temperature required for full ionization, the hydrogen gas is not fully ionized throughout the compression cycle. We therefore use the Saha equation²⁴ to calculate the EOS for the hydrogen plasma. Although the Saha equation may not be appropriate for hydrogen beyond solid density, the model is well justified since the Fermi energy is much smaller than the thermal energy.

We use power-law approximations based on SESAME opacity library for calculating the Rosseland mean free path in the solids, i.e.,

$$L_R = A \rho^\alpha T^\beta, \quad (9)$$

where A , α and β are chosen to fit the SESAME opacity curves in the region of $T \leq 10$ eV. Thermal conduction in the solid in this temperature regime is still dominated by electron thermal conduction, because the photon mean free path is much shorter than the electron mean free path. Since most temperatures in solids are below 10 eV, simulation results are not sensitive to this parameterization.

Photon absorption in hydrogen is dominated by shell absorption at temperatures below 10 eV. Since there is no analytical expression for opacity in this temperature regime, we use a Maxwellian distribution function to fit the Rosseland opacity curves for hydrogen in the SESAME opacity library for temperatures under 20 eV. Above 20 eV, we use bremsstrahlung¹⁷ absorption cross sections to calculate the opacity.

iii) Pressure due to Magnetic Field

The system circuit for a solid liner compression can be schematically expressed as a simple RLC circuit shown in Fig. 1. The resistance R is considered to be constant throughout the compression cycle. If the liner inductance is constant in time, the current can be analytically expressed as

$$I(t) = CV_0 \frac{A^2 + B^2}{B} e^{-At} \sin Bt, \quad (10)$$

where V_0 is the initial voltage of the capacitor bank,

$$A = \frac{R}{2L} \quad \text{and} \quad B = \left(\frac{1}{LC} - \frac{R^2}{4L^2} \right)^{1/2}. \quad (11)$$

However, since L is a function of the liner position, the circuit equation is coupled with the equation-of-motion. We have adjusted R , L , C from their initial values to compensate for the time-varying inductance in the system. The following parameters for a cylindrical implosion experiment⁶ have been used in this calculation: $R = 1 \text{ m}\Omega$, $C = 1300 \mu\text{F}$, $L = 30 \text{ nH}$ (combined inductance of circuit and liner).

The diffusion time scale for the magnetic field in the liner is

$$\tau_B = \sigma_L \mu_L \Delta r^2. \quad (12)$$

From CALE, the average liner temperature at peak compression is less than 1 eV. Using $\sigma_L = 10^7 \text{ ohm}^{-1}\text{m}^{-1}$ for the conductivity at $T = 0.6 \text{ eV}$, $\mu_L = 4\pi \times 10^{-7} \text{ Hm}^{-1}$ for the magnetic permeability of the liner, and $\Delta r = 1 \text{ mm}$ for the liner thickness, from Eq. (12) the diffusion time scale is 50 μsec , which is relatively long compared to the compression time, (13 μsec). This estimate agrees with

CALE's result which shows that 10 μ sec is required for the current to diffuse across 1/4 of the liner thickness. Therefore, it is reasonable to approximate the spatial current distribution in the liner with a surface current.

The magnetic pressure due to a surface current through the liner is nonuniform along the polar angle direction for the spherical compression, and can be expressed as

$$P_B = \frac{B_\phi^2}{2\mu_0}, \quad (13)$$

where $B_\phi = \frac{\mu_0 I}{2\pi r_1 \sin \theta}$ (14)

is the azimuthal component of the magnetic field, I is the time-varying current running through the liner, r_1 is the radial position of the liner outer surface, θ is the polar angle measured around the electrode symmetry axis z , and μ_0 is the magnetic permeability in vacuum. Since HYDRAD is a one-dimensional code, it can only compute a single value for the magnetic pressure. To account for the tapered liner thickness, HYDRAD uses an average thickness for the liner. The average magnetic pressure is

$$P_B = 1.247 \times \frac{B_{\phi 0}^2}{2\mu_0}, \quad (15)$$

where $B_{\phi 0} = \frac{\mu_0 I}{2\pi r_1}$ (16)

B. CALE

The version of CALE used for the simulation has the following features:

- 2-D MHD calculation in Eulerian coordinates or Lagrangian coordinates,
- elastic properties of materials,
- Saha equation for the equation-of-state and conductivity of hydrogen,
- polynomial function input for the EOS of solids,
- frictionless contact between liner and electrode,

-- and no thermal radiation or conduction in the system.

A fully Eulerian calculation is chosen for the simulations in order to correctly treat details at complicated boundaries.

The conductivities of the aluminum and gold are parametrized by a four-phase model. The solid, liquid and vapor conductivities are parametrized as a power law dependence on temperature and density. The plasma conductivity is calculated using the Thomas-Fermi ionization state, rather than the Saha ionization, since the plasma states of interest are nearly degenerate.

Parameters for the EOS for the solids were taken from Ref. 14, while the EOS from the SESAME library was used to obtain parameters appropriate for the higher pressures encountered in the gold target. The strength properties of the metals is based on the Steinberg-Guinan model.

C. Limit of Energy Deposition

The fraction of the 5.3 MJ of stored energy which is available for compression is of crucial importance for the microfission experiment. An upper limit to the amount of energy which can be converted to compression is obtained from the work-energy relation,

$$\Delta U = \int_{r_0}^{r_p} F_B dr = \int_{r_0}^{r_p} \left[-2 \ln \tan \frac{\theta_m}{2} \right] \frac{\mu_0 I^2(t)}{4\pi} dr, \quad (17)$$

where r_0 is the initial position of the outer liner surface, r_p is the radius of the liner outer surface at peak compression, and $\theta_m = \pi/4$ is the electrode angle. Since most of the displacement Δr occurs at the time when $I(t)$ is close to the maximum, Eq. (17) can be written as

$$\Delta U_{\max} (\text{MJ}) \approx 1.8 \times 10^{-3} (r_0 - r_p) I_{\max}^2 (\text{MA}), \quad (18)$$

where I_{\max} is the maximum value of $I(t)$. Equation (18) shows the fundamental limitation on the efficiency for energy conversion. For example, using $r_0 = 4.15$ cm, $r_p = 1.5$ cm, and $I_{\max} = 16$ MA (90 KV discharge), the maximum energy available for compression is 1.2 MJ. From Eq.

(18), the efficiency for energy conversion is 22 % (1.2/5.3), which agrees with the prediction from CALE (19 %).

III. Results of Simulations

The geometry used in HYDRAD simulations is schematically shown in Fig. 2. The total number of Lagrangian cells is 40. The region containing the liner, working fluid and target is divided into a continuous 15 (in z) \times 100 (in r) Eulerian grid in CALE. A fine grid (15 polar sectors, 13 radii) is used to describe the target to facilitate the subsequent simulation of nuclear reactions. Except for the center of the target, all cells are quadrilaterals. A typical run requires \approx 0.5 hour for HYDRAD without radiation, and \approx 15 hours for CALE in Central Processor Unit (CPU) time on a DECstation 3100.

Initial conditions for 4 cases simulated are listed in Table I. In this section, we show results of both 1-D (HYDRAD) and 2-D (CALE) simulations.

A. Without Radiation

Since the liner is tapered (see Fig. 1), we take the average thickness of 1.5 mm as the initial thickness of the liner. This leads to a 1-D liner mass of 59 gm, as compared to the actual mass of 51 gm used by CALE. Figure 1 shows that the liner and the plasma occupy an angle of $\pi/2$ radians in the θ direction, whereas the target subtends an angle of π radians. The target, which subtends an angle from $\pi/4$ to $3\pi/4$ in Fig. 2, contains 71 % of the full target volume. Therefore, the target radius is increased by a factor of 1.12 to simulate a target of the same mass. The target in all HYDRAD simulations has a mass of 27 grams, and a radius of 0.783 cm.

Figure 3 shows target pressure, density and temperature, spatially averaged at peak compression, as a function of the initial plasma pressure from HYDRAD and CALE simulations. The average target densities from HYDRAD simulations range from 38 gm/cm³ to 43 gm/cm³, while from CALE simulations range from 34 gm/cm³ to 40 gm/cm³, as the initial pressure ranges

from 71 bar (case A) to 952 bar (case D). At initial plasma pressures below 256 bar (case C), the average target density at peak compression is almost constant ($\approx 42 \text{ gm/cm}^3$) from 1-D, and $\approx 39 \text{ gm/cm}^3$ from 2-D. With the initial pressure at 952 bar (case D), the target density is 8 % less than in cases A-C. These results clearly show an inverse correlation between density and initial plasma pressure. However, there is a trade-off for increasing the liner momentum, i.e., a greater liner momentum may create a stronger shock wave in the target, which may increase thermal energy at the expense of compression energy, leading to lower target density.

Average target densities from CALE at peak compression are consistently lower than from HYDRAD by 3 - 4 gm/cm^3 . This density difference may be attributed to nonuniform compression in the 2-D simulation. Because of the cylindrical symmetry of the liner, the radial compression wave converges earlier at the equator ($z = 0$) than the axial compression wave at the axis ($r = 0$). The compression of the target in CALE is more nearly cylindrical than spherical. This also explains why the target at peak compression appears prolate, as will be seen in Fig. 4. Therefore, the compression wave in CALE is less focused than in HYDRAD, giving rise to smaller average target densities.

Two-dimensional density profiles at peak compression from CALE are shown in Fig. 4. As seen, the lower the initial plasma pressure, the closer the liner gets to the target. This is especially true in cases B, C and D. The bubbles seen in B, C and D in the plasma near the equator are most likely caused by the local imbalance of plasma and magnetic pressure, less likely by an instability. The magnetic pressure is not uniform along the θ direction and is lowest at the equator ($z=0$), as Eq. (14) shows. The plasma pressure, which is nearly uniform, exceeds the magnetic pressure earlier in time at the equator than for regions closer to the pole. A bubble is developed as the net force near the equator pushes outward. In case D, a large bubble has been formed in the liner due to early development of high pressure in the plasma. As seen by the contour lines, higher initial plasma pressure results in more nearly adiabatic and uniform target compression. The density gradients for case D are much smaller than those for cases A, B and C, and the contours are more

spherical than cylindrical. Referring back to Fig. 3, the target temperature for case D is low, indicating that target compression is more nearly adiabatic.

The CALE simulation indicates that some interesting physics is occurring as the liner flows past the 45 degree electrode corner. The following information is provided by CALE: time, 9.5 microseconds; speed of liner near electrode, 0.8 cm/ μ sec, speed of sound in liner, 0.7 cm/ μ sec; temperature of liner, 1.1 eV for $r < 0.8$ cm, 0.17 eV for $r > 0.8$ cm; and pressure in the liner, 320 kbar for $r < 0.8$ cm and 220 kbar for $r > 0.8$ cm.

The liner gets very hot as it moves past the electrode corner. The speed indicated above suggests that a separation between the liner and electrode might occur. However, no indication of this separation is observed in CALE, possibly because the region of possible separation is small compared to the grid size of 0.6 cm (radial) by 0.3 cm (axial) in this area. Radiographs from the recent experiment at SHIVA Star confirm that the liner is in contact with the electrode at this point.

One-dimensional shock wave motion in the target can be seen in Fig. 5, which shows radial profiles of pressure, density and temperature at different times close to peak compression for case A. Initially, the magnitude of the shock pressure in the target is approximately 5 Mbar, about the same as the plasma pressure. The momentum of the target surface compresses the target interior, until the pressure gets up to 35 Mbar at the center and rebounds. Time histories of the average target pressure, density and temperature from HYDRAD for case A are shown in Fig. 6. The compression process takes about 1 μ sec, and the dwell time for which the average target density is above 35 gm/cm³ is about 700 nsec.

The plasma pressure at peak compression from HYDRAD ranges from 2.17 Mbar to 3.32 Mbar as shown in Table II. The temperature reaches above 100 eV for cases A and B; bremsstrahlung radiation from these hot dense plasmas may have significant influence on compression. For instance, the preheating of the target surface may reduce shock wave compression in the target. On the other hand, loss of plasma pressure at early times may increase

maximum liner momentum, thus causing a high plasma pressure at peak compression. These two competing mechanisms can affect compression in either way.

Table III shows plasma conditions at peak compression from CALE. Plasma pressures are 2-4 Mbar, which are close to HYDRAD values. However, CALE's temperatures are about 1.2 - 1.5 times higher than HYDRAD's. Since thermal conduction is not included in either calculation, this behavior suggests that viscous heating in CALE's plasma is quite significant.

The distribution of energy at peak compression from HYDRAD for all cases is shown in Table IV. The internal energy in solids is defined as the sum of 1) degenerate electron energy (compression energy) 2) ionization energy, and 3) ion thermal energy. The total energy deposited in the system is \approx 1.2 MJ and is consistent with Eq. (18). The target energy is \approx 20 % of the total energy deposition. Most of the energy is deposited in the liner, and about 30% - 50% of the total energy is in solids in the form of thermal energy. Energy of \approx 100 to 200 KJ is deposited in the target as degenerate electron energy which is the energy accounted for by compression. Therefore, about 4 % of the capacitor energy is delivered into the target in the form of compression work.

For comparison, the energy distribution in each component from CALE for case A is shown in Table V. The total energy input is around 1 MJ, and \approx 20 % of the total energy input is deposited in the target. Again, this result agrees with HYDRAD.

Table VI lists HYDRAD and CALE results for case A (2 eV, 1×10^{19} cm⁻³ initial plasma conditions.) The time at peak compression is about 13 μ sec for both cases. CALE has a higher local pressure and density, although the average target pressure and density are higher in HYDRAD. The highest pressure in the CALE simulation usually occurs on the z axis, i.e., the center of the compression. CALE's higher local quantities in Table VI may be due to the smaller radial grid size at the axis, which reveals more detailed structure of local quantities. Therefore, CALE's local pressure appears higher than HYDRAD's. Time histories of average pressure,

density and temperature from CALE for case A are shown in Fig. 7. The dwell time for the average target density above 35 gm/cm^3 is about 500 nsec and comparable with HYDRAD.

B. With Radiation

Spatially averaged target quantities with radiation at peak compression from HYDRAD are shown in Fig. 8. For comparison, results without radiation from HYDRAD are also shown. The average target density increases as the initial plasma pressure decreases, which is similar to the trend seen without radiation. Therefore, a lower initial plasma pressure is more desirable.

The temperature in the target is generally higher with radiation than without radiation, as is the pressure. Target densities are lower in cases A-C and higher in D with radiation than without radiation. This shows that the role of radiation is complex. As discussed earlier, there are two competing mechanisms: 1) preheating of the target surface and 2) loss of pressure in the hydrogen plasma, affecting target compression. These two mechanisms may lead to changes in target density, in either positive or negative directions. The effect of preheating depends more upon thermal conduction inside the target, while pressure loss depends more upon heat transfer at the boundary surface of the plasma. As the radiation loss in the plasma increases and thermal conduction inside the target remains unchanged, effects from pressure loss in the plasma will dominate over effects from preheating. Since the pressure loss leads to increased momentum in the liner, the target density is increased at peak compression. This explains why the average target density in case D increases, while the others decrease due to thermal radiation.

Plasma quantities at peak target compression are shown in Fig. 9. As seen, plasma temperatures in all cases are significantly lower with than without radiation. Correspondingly, plasma densities are higher with radiation than without radiation as a result of resisting the inward motion of the liner. Plasma densities in some cases are higher than solid density. However, since the Fermi energy at densities of $\approx 0.1 \text{ gm/cm}^3$ is around 5 eV, which is smaller than the plasma temperature ($\approx 20 \text{ eV}$), use of the Saha equation is well justified.

Figure 10 shows the time history of average target pressure, density and temperature for case A. The histories are similar to results without radiation, despite significant differences in plasma properties when radiation is included. The dwell time for average target density above 35 gm/cm^3 is around 700 nsec. Because of radiation loss, the liner speed is faster with than without radiation. Peak compression times in all four cases are earlier by tens of nanoseconds due to radiation. Note that the target temperature is increased by about 0.5 - 1 eV due to the radiation.

The energy distribution with radiation from HYDRAD is shown in Table VII. Comparing Table VII with Table IV, all internal energies in the target are increased to $\approx 320 \text{ KJ}$. The increased energy raises the target temperature, instead of increasing the target density, in cases A-C. The total energy deposited in the system is around 1.25 MJ, which is close to that without radiation.

IV. Summary

In this study, the 1-D hydrodynamics code HYDRAD and the 2-D MHD code CALE are used to simulate compression of a hydrogen working fluid and target. It is found that the 1-D and 2-D results without radiation are comparable. The 1-D calculation is much less time consuming than the 2-D ($\approx 1:30$ in CPU time), and includes important physics, i.e., thermal radiation, which is not available in our version of CALE. Although the 1-D model simplifies several important physics topics, for instance, circuit coupling and current diffusion, efforts have been made to minimize differences between the 1-D and 2-D results caused by these approximations. In the absence of a complete 2-D code, HYDRAD is a very efficient and useful tool for simulating liner and target compressions.

The results are as follows:

- a) the time for peak compression of a 27 gram gold target is $12.5 \mu\text{sec} - 13.5 \mu\text{sec}$;
- b) the dwell time for an average target density above 35 gm/cm^3 ranges from 500 nsec (2-D) to 700 nsec (1-D);

- c) an average target density (pressure) of about 40 gm/cm^3 (12 Mbar) and a maximum local density (pressure) of $60-100 \text{ gm/cm}^3$ (30-140 Mbar) can be achieved in the target using 5.3 MJ of energy from SHIVA Star;
- d) an energy of 1.2 MJ is deposited in the liner, plasma and target, including 200 - 350 KJ in the target;
- e) radiation brings down the plasma temperature consistently to around 20 eV and increases the target temperature by about 0.5 - 1 eV; however, it has little influence on the average target density and pressure at peak compression; and
- f) to obtain a higher target density, a lower initial plasma pressure is more desirable.

REFERENCES

1. A. E. Sherwood, E. L. Cantvel, C. A. Ekdhal, I. Henins, H. W. Hoiday, T. R. Jarboe, P. L. Klinger, R. C. Malone, J. Marshall, and G. A. Sawyer, *Megagauss Physics and Technology*, edited by P. J. Turchi (Plenum Press, New York, 1980), p. 375.
2. P. J. Turchi, A. L. Cooper, R. D. Ford, D. J. Jenkins, and R. L. Burton, in *Megagauss Physics and Technology*, edited by P. J. Turchi (Plenum Press, New York, 1985), p. 375.
3. S. G. Alikhanov, V. P. Bakhtin, and D. A. Toporkov, in *Ultrahigh Magnetic Fields-Physics, Techniques, Applications*, edited by V. M. Totov and G.A. Shvetsov (Moscow "Nauka", 1984), p. 213.
4. A. G. Eskov, M. I. Kitayev, and R. Kh. Kurtmullayev, in *Ultrahigh Magnetic Fields-Physics, Techniques, Applications*, V. edited by V. M. Totov and G.A. Shvetsov (Moscow "Nauka", 1984), p. 204.
5. A. A. Petrukhin, N. P. Bidlyo, S. F. Garanin, V. M. Danov, V. V. Zmushko, A. I. Kuzyaev, V. N. Mokhov, E. S. Pavlovskii, V. A. Prokopov, V. K. Chernyshev, V. A. Shvetsov, and V. B. Yakubov, in *Ultrahigh Magnetic Fields-Physics, Techniques, Applications*, edited by V. M. Totov and G.A. Shvetsov (Moscow "Nauka", 1984), p. 406.
6. J. H. Degnan, M. L. Alme, W. L. Baker, J. S. Buff, C. B. Boyer, C. J. Clouse, S. K. Coffey, D. W. Conley, D. Dietz, J. D. Graham, S. L. Gonzalez, K. E. Hackett, D. J. Hall, J. L. Holmes, E. A. Lopez, W. F. McCullough, D. W. Price, R. E. Reinovsky, N. F. Roderick, P. J. Turchi, and J. M. Welby, in *Megagauss Technology and Pulsed Power Applications*, edited by C. M. Fowler, R. S. Caird, and E. J. Erickson (Plenum Press, New York, 1987), p. 699-706.

7. J. H. Degnan, W. L. Baker, J. D. Beason, C. J. Clouse, D. Dietz, D. J. Hall, J. L. Holmes, D. W. Price, and C. R. Sovinec, in *Megagauss Technology and Pulsed Power Applications*, edited by V. M. Titov and C. A. Shvetsov (Plenum Press, New York, 1990), p. 623-630.
8. N. A. Krall and A. W. Trivelpiece, *Principles of Plasma Physics*, (McGraw Hill, New York, 1973).
9. B. Chen, T. A. Armstrong, R. A. Lewis, R. Newton, G. A. Smith, J. P. Bocquet, F. Malek, H. Nifenecker, M. Maurel, E. Monnand, P. Perrin and C. Ristori, G. Ericsson, T. Johansson, G. Tibell, M. Rey-Campagnolle, S. Polikanov, T. Krogulski and J. Mougey, *Phys. Rev. C* **45**, 2332 (1992).
10. E. D. Minor, T. A. Armstrong, R. Bishop, V. Harris, R. A. Lewis, G. A. Smith, *Z. Phys. A* **336**, 461 (1990).
11. R. A. Lewis, G. A. Smith, R. J. Kanzleiter, K. I. Higman and R. Newton, *Fusion Tech.* **20**, No. 4, Part 2, 1046 (1991).
12. R. A. Lewis, R. Newton, G. A. Smith and R. J. Kanzleiter, *Nuc. Sci. Eng.* **109**, 411 (1991).
13. P-R. Chiang, 'HYDRAD - One-Dimensional Radiative Hydrodynamics Code,' Laboratory for Elementary Particle Science, The Pennsylvania State University, 1993 (unpublished).
14. CALE users manual, July 1, 1991, Robert Tipton, LLNL, Mail Stop L-35, P.O. Box 808 Livermore, CA 94550; *Megagauss Technology and Pulsed Power Applications*, Eds. C. M. Fowler, R. S. Cavid and D. J. Erickson, (Plenum Press, New York, 1987), p. 299.
15. F.M. Lehr, A. Alaniz, J. D. Beason, L. C. Carswell, J. H. Degnan, J. F. Crawford, S. E. Englert, T. J. Englert, J. M. Gahl, J. H. Holmes, T. W. Hussey, G. F. Kiutu, B. W. Mullins, R. E. Peterkin, Jr., N. F. Roderick, P. J. Turchi and J. D. Graham, 'Formation of

Plasma Working Fluid for Compression by Liner Implosions,' submitted to Journal of Applied Physics.

16. F. M. Lehr, J. H. Degnan, D. Dietz, S. E. Englert, T. J. Englert, T. W. Hussey, G. F. Kiuttu, J. M. Messerschmitt, B. W. Mullins, C. A. Outten, R. E. Peterkin, Jr., N. F. Roderick, P. J. Turchi and J. D. Graham, 9-th IEEE Pulsed Power Conference, June 6-10, 1993.
17. Ya. B. Zel'dovich and Yu. P. Raizer, *Physics of Shock Waves and Temperature Hydrodynamic Phenomenon* (Academic Press, New York, 1966).
18. P. Collela and P. R. Woodard, *J. Comp. Phys.* **54**, 174 (1984).
19. P. R. Woodard and P. Collela , *J. Comp. Phys.* **54**, 115 (1984).
20. T. Tajima, *Computational Plasma Physics: With Applications to Fusion and Astrophysics* (Addison-Wesley, New York, 1989).
21. N. A. Tahir and K. A. Long, *Laser and Particle Beams* **4**, 287 (1986).
22. J. P. Christiansen, D.E.T.F. Ashby and K.V. Roberts, *Comp. Phys. Comm.* **7**, 271 (1974).
23. S. P. Lyon and J. D. Johnson, LA-UR-92-3407 (1992).
24. J. A. Bittencourt, *Fundamentals of Plasma Physics*, (Pergamon Press, New York, 1988).

Table I. Initial plasma conditions for simulations. All cases have a 27 gram gold target at the center, and the liner and target are initially at room temperature.

Case	Density	Temperature (eV)	Pressure (bar)
A	10^{19} cm^{-3} ($1.67 \times 10^{-5} \text{ g/cm}^3$)	2	71
B	10^{19} cm^{-3} ($1.67 \times 10^{-5} \text{ g/cm}^3$)	5	161
C	$6 \times 10^{19} \text{ cm}^{-3}$ ($1 \times 10^{-4} \text{ g/cm}^3$)	2	256
D	$6 \times 10^{19} \text{ cm}^{-3}$ ($1 \times 10^{-4} \text{ g/cm}^3$)	5	952

Table II. Plasma conditions at peak compression from HYDRAD without radiation.

Case	Plasma pressure (Mbar)	Plasma temperature (eV)	Plasma density (gm/cm ³)
A	3.32	138	0.0125
B	3.11	263	0.00613
C	2.91	57	0.0266
D	2.17	110	0.0102

Table III. Plasma conditions at peak compression from CALE.

Case	Plasma pressure (Mbar)	Plasma temperature (eV)	Plasma density (gm/cm ³)
A	3.7	220	0.009
B	2.7	350	0.0040
C	2.4	76	0.0332
D	1.4	128	0.0057

Table IV. Energy distribution in the system at peak compression from HYDRAD without radiation.

	Case A	Case B	Case C	Case D
Internal energy in target	290 KJ	248 KJ	222 KJ	121 KJ
Internal energy in plasma	124 KJ	238 KJ	306 KJ	597 KJ
Internal energy in liner	780 KJ	709 KJ	657 KJ	399 KJ
Kinetic energy in target	3 KJ	3 KJ	2 KJ	1 KJ
Kinetic energy in plasma	≈ 0.04 J	0.2 J	24 J	9 J
Kinetic energy in liner	51 KJ	56 KJ	66 KJ	100 KJ
Total energy	1.25 MJ	1.25 MJ	1.25 MJ	1.22 MJ

Table V. Energy distribution in the system at peak compression from CALE.

	Case A	Case B	Case C	Case D
Internal energy in target ^a	221 KJ	192 KJ	206 KJ	89 KJ
Internal energy in plasma	114 KJ	243 KJ	149 KJ	368 KJ
Internal energy in liner ^a	616 KJ	486 KJ	591 KJ	358 KJ
Kinetic energy in target	13 KJ	2 KJ	11 KJ	1 KJ
Kinetic energy in plasma	2 J	3 J	11 J	300 J
Kinetic energy in liner	38 KJ	35 KJ	50 KJ	79 KJ
Total energy	1002 KJ	958 KJ	1017 KJ	895 KJ

^a The energy of degenerate electrons has been estimated by using the cold-temperature EOS from the TFC model and included in the internal energy.

Table VI. Comparison between HYDRAD and CALE for case A.

Parameters	HYDRAD	CALE
Initial plasma conditions	2 eV, $1 \times 10^{19} \text{ cm}^{-3}$	2 eV, $1 \times 10^{19} \text{ cm}^{-3}$
Target	27 gm Au	27 gm Au
Initial target radius	0.783 cm	0.682 cm
Maximum current	= 16 MA	\approx 16 MA
Peak compression time	12.81 μsec	12.99 μsec
Plasma P at peak	\approx 3.3 Mbar	\approx 3.6 Mbar
Plasma T at peak	\approx 135 eV	\approx 221 eV
Maximum target P at peak	\approx 34 Mbar	\approx 147 Mbar
Maximum target ρ at peak	\approx 60 gm/cm ³	\approx 94 gm/cm ³
Maximum target T at peak	\approx 4.8 eV	\approx 11.8 eV
Average target P at peak	\approx 11.3 Mbar	\approx 10 Mbar
Average target ρ at peak	\approx 43 gm/cm ³	\approx 40 gm/cm ³
Average target T at peak	\approx 2.2 eV	\approx 1.7 eV
Average liner ρ at peak	\approx 6.0 gm/cm ³	\approx 4.2 gm/cm ³
Average liner T at peak	\approx 0.3 eV	< 1 eV

Table VII. Energy distribution in the system at peak compression from HYDRAD with radiation.

	Case A	Case B	Case C	Case D
Internal energy in target	344 KJ	342 KJ	322 KJ	320 KJ
Internal energy in plasma	18 KJ	18 KJ	144 KJ	147 KJ
Internal energy in liner	834 KJ	841 KJ	730 KJ	726 KJ
Kinetic energy in target	4 KJ	4 KJ	3 KJ	2 KJ
Kinetic energy in plasma	≈ 0.005 J	0.02 J	0.32 J	42 J
Kinetic energy in liner	49 KJ	46 KJ	54 KJ	63 KJ
Total energy	1.25 MJ	1.25 MJ	1.25 MJ	1.26 MJ

LIST OF FIGURES

Fig. 1. Schematic of spherical solid liner at Shiva Star.

Fig. 2. Schematic of system geometry in one dimensional simulation of compression.

Fig. 3. Average target pressure, density and temperature at peak compression vs. initial plasma pressure from HYDRAD.

Fig. 4. System geometries and density contours in the target at peak compression for cases A-D (see Table I) from CALE.

Fig. 5. Radial profiles of pressure, density, and temperature at different times close to the peak compression from HYDRAD for case A.

Fig. 6. Time history of average pressure, density, and temperature in the target from HYDRAD without radiation for case A.

Fig. 7. Time history of average pressure, density, and temperature in the target from CALE without radiation for case A.

Fig. 8. Average target pressure, density and temperature at peak compression vs. initial plasma pressure from HYDRAD with and without radiation.

Fig. 9. Average plasma pressure, density and temperature at peak compression vs. initial plasma pressure from HYDRAD with and without radiation.

Fig. 10. Time history of average pressure, density, and temperature in the target from HYDRAD with radiation for case A.

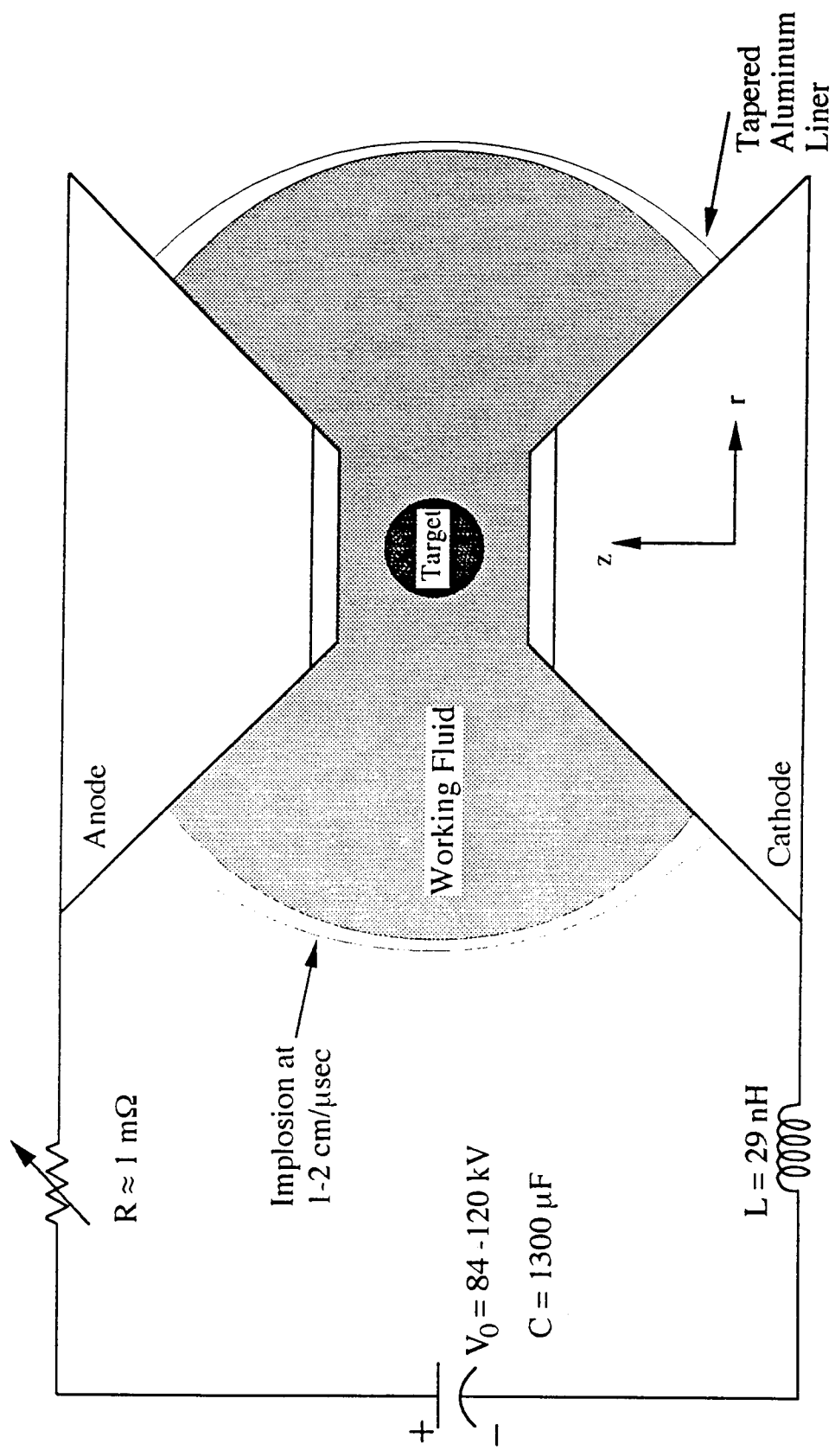
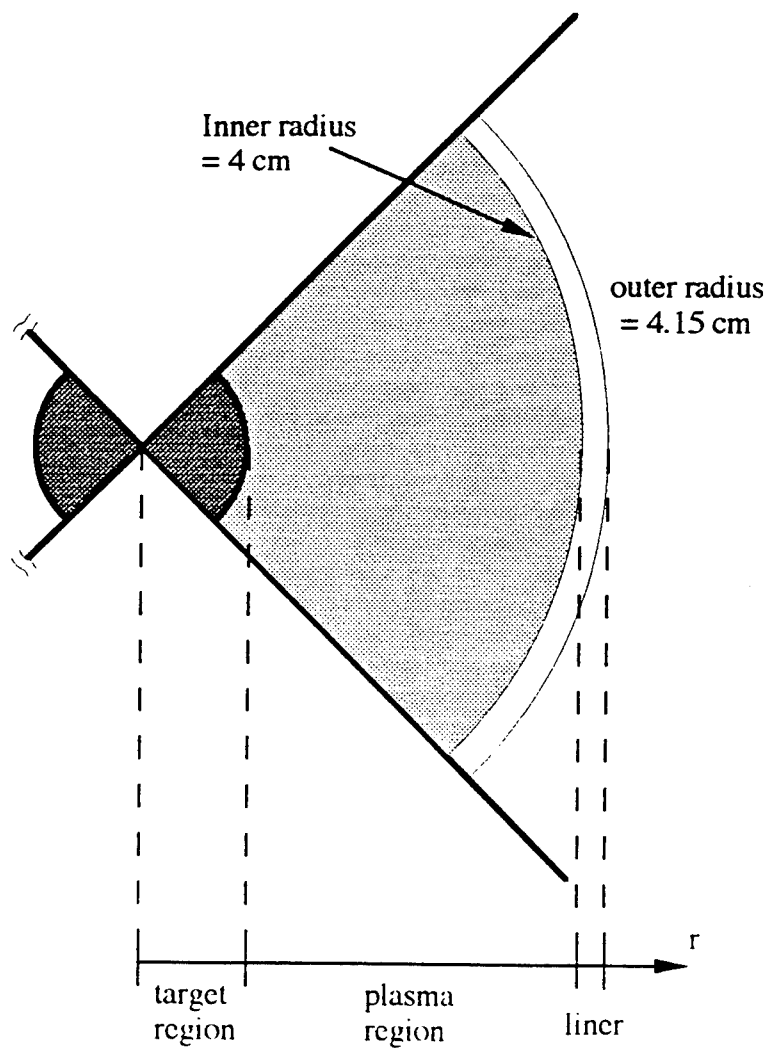


Fig. 1.



number of Lagrangian cells	12	4	24
----------------------------	----	---	----

Fig. 2.

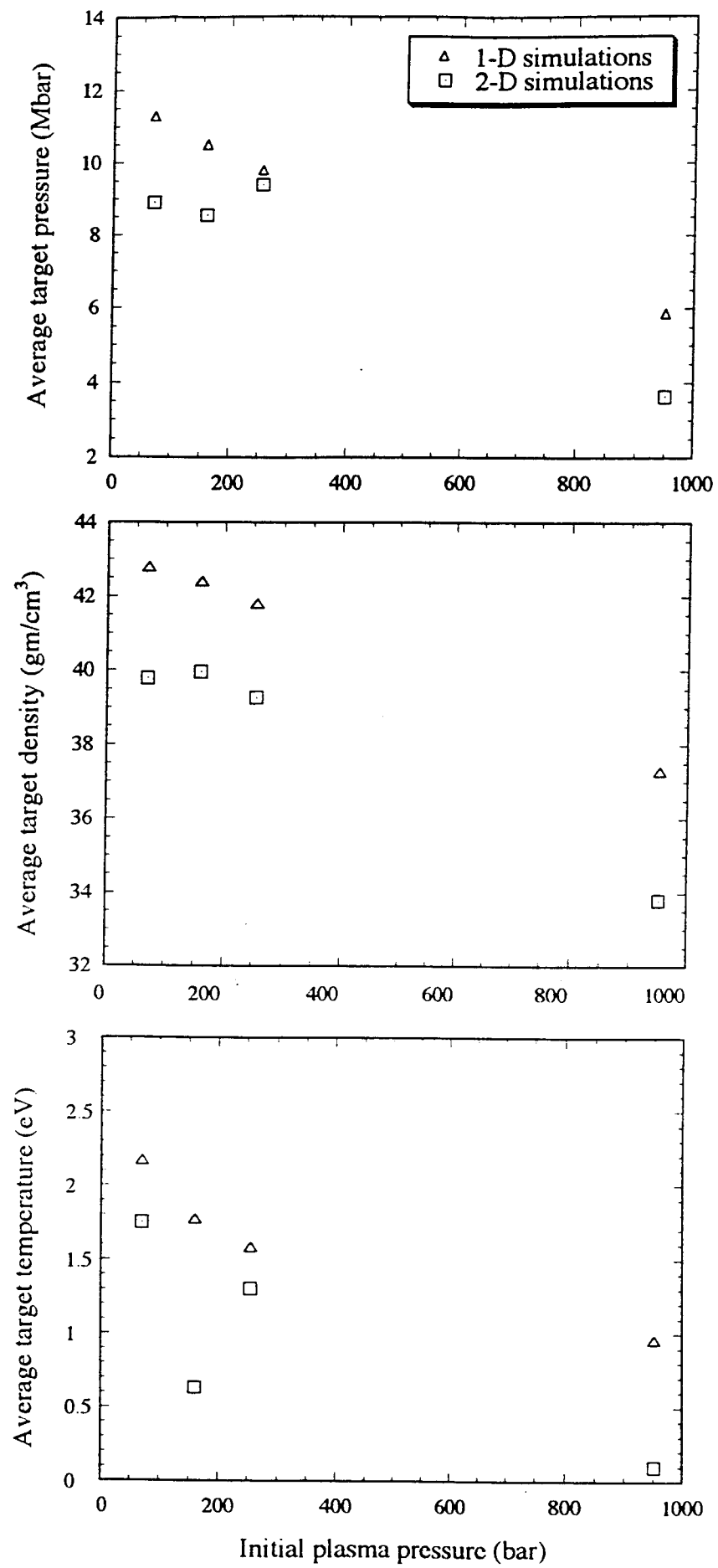
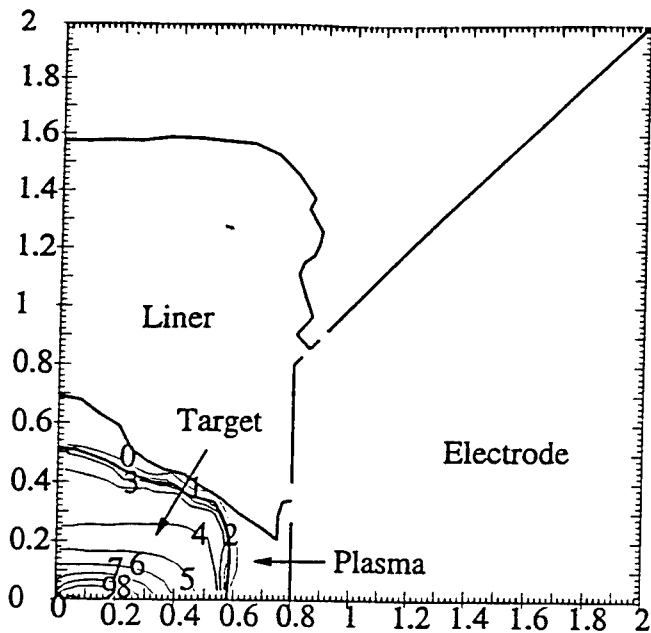
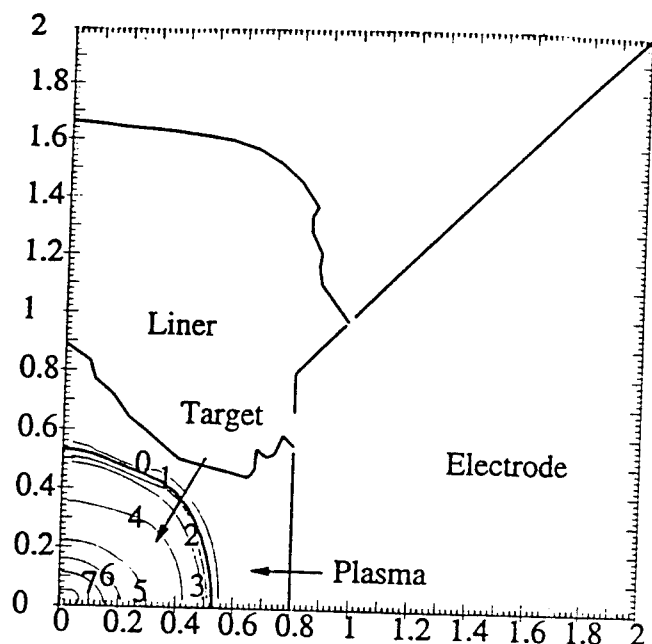


Fig. 3

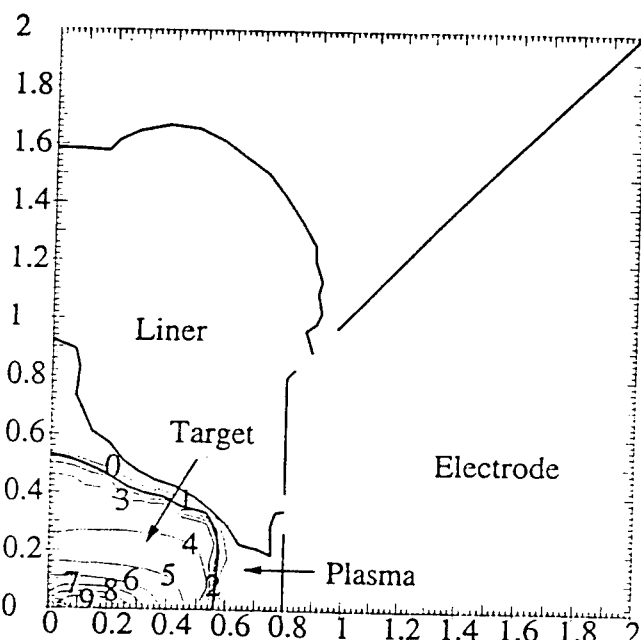
Case A



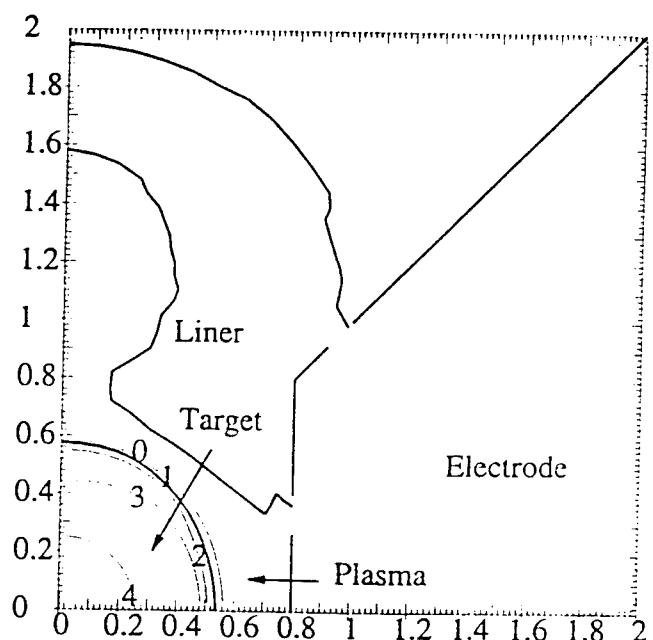
Case C



Case B



Case D



r (cm)
 z (cm)

Contour	Density (gm/cm^3)
0	8.0
1	16.0
2	24.0
3	32.0
4	40.0
5	48.0
6	56.0
7	64.0
8	72.0
9	80.0

Fig. 4

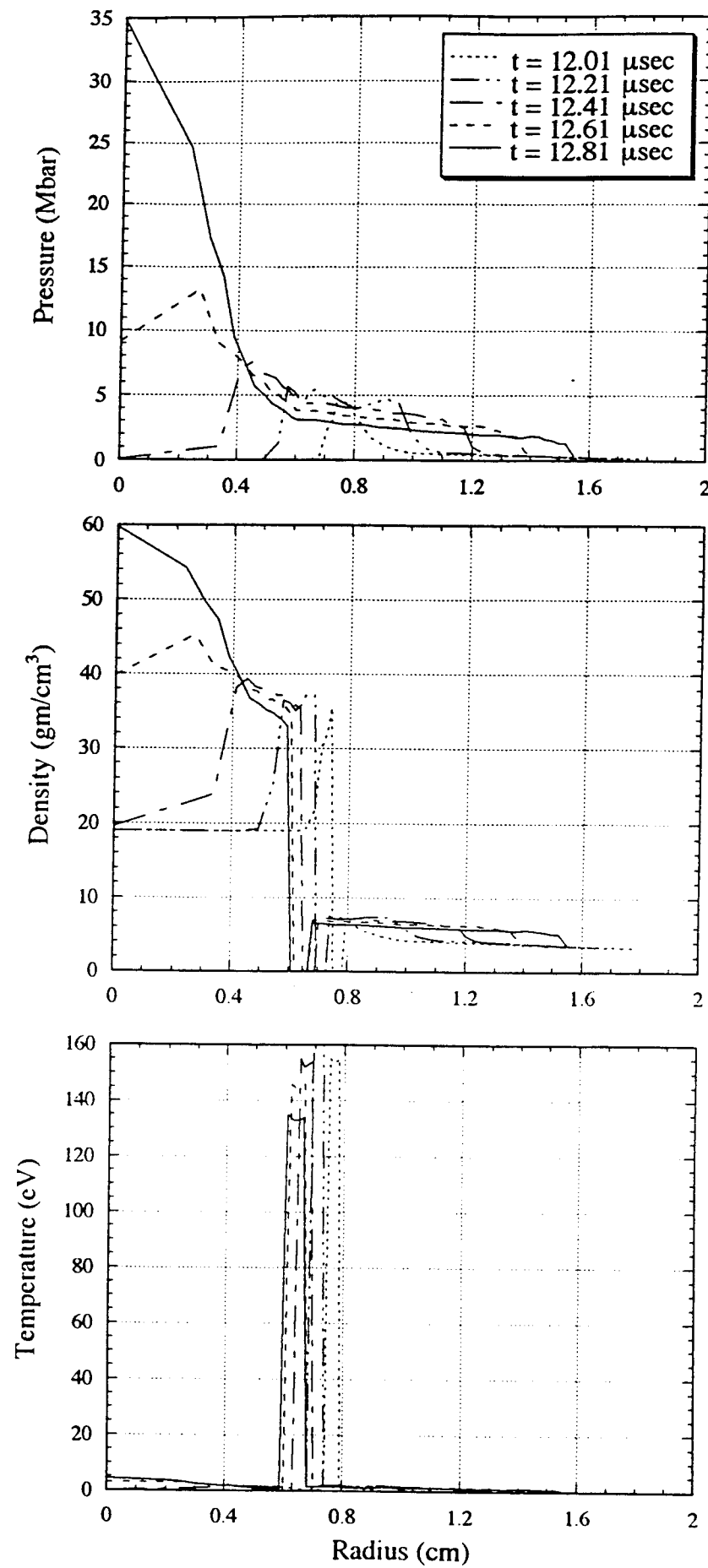


Fig. 5

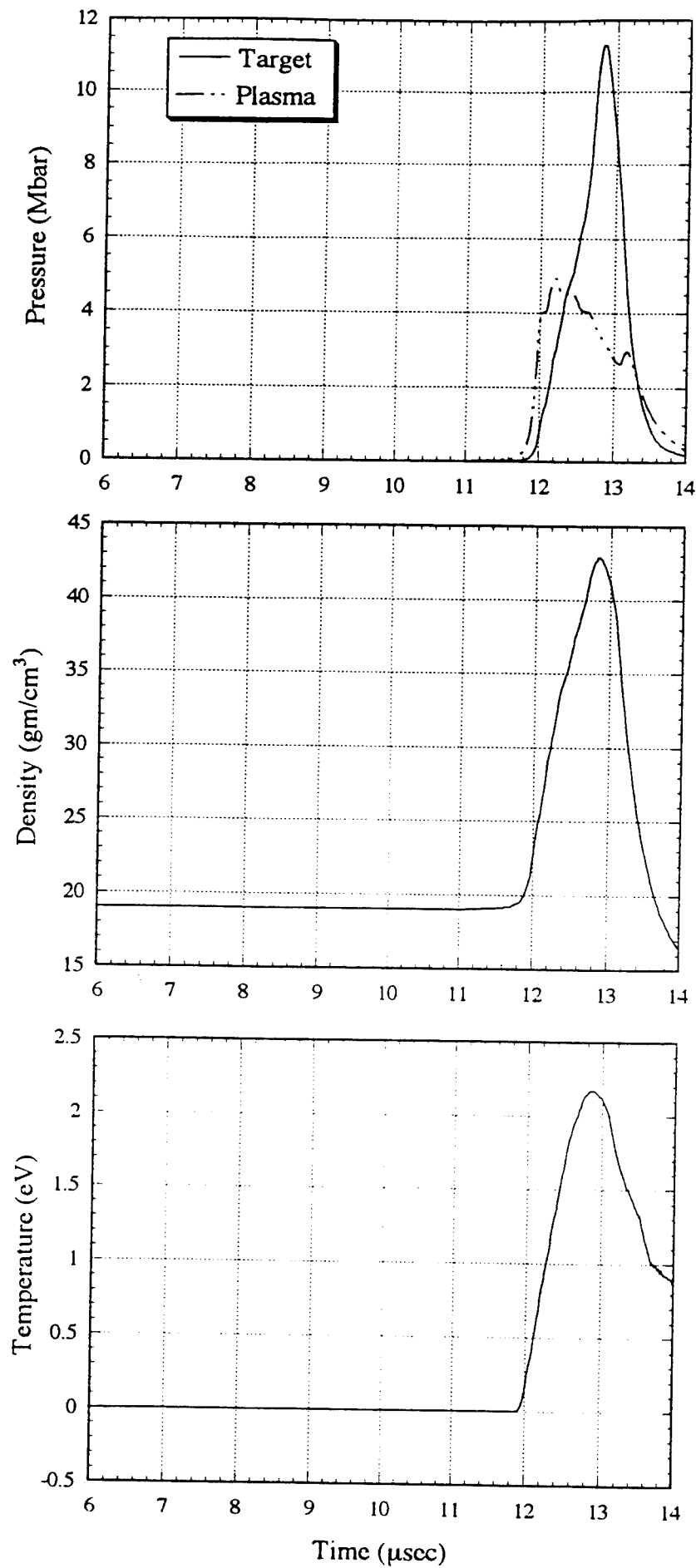


Fig. 6

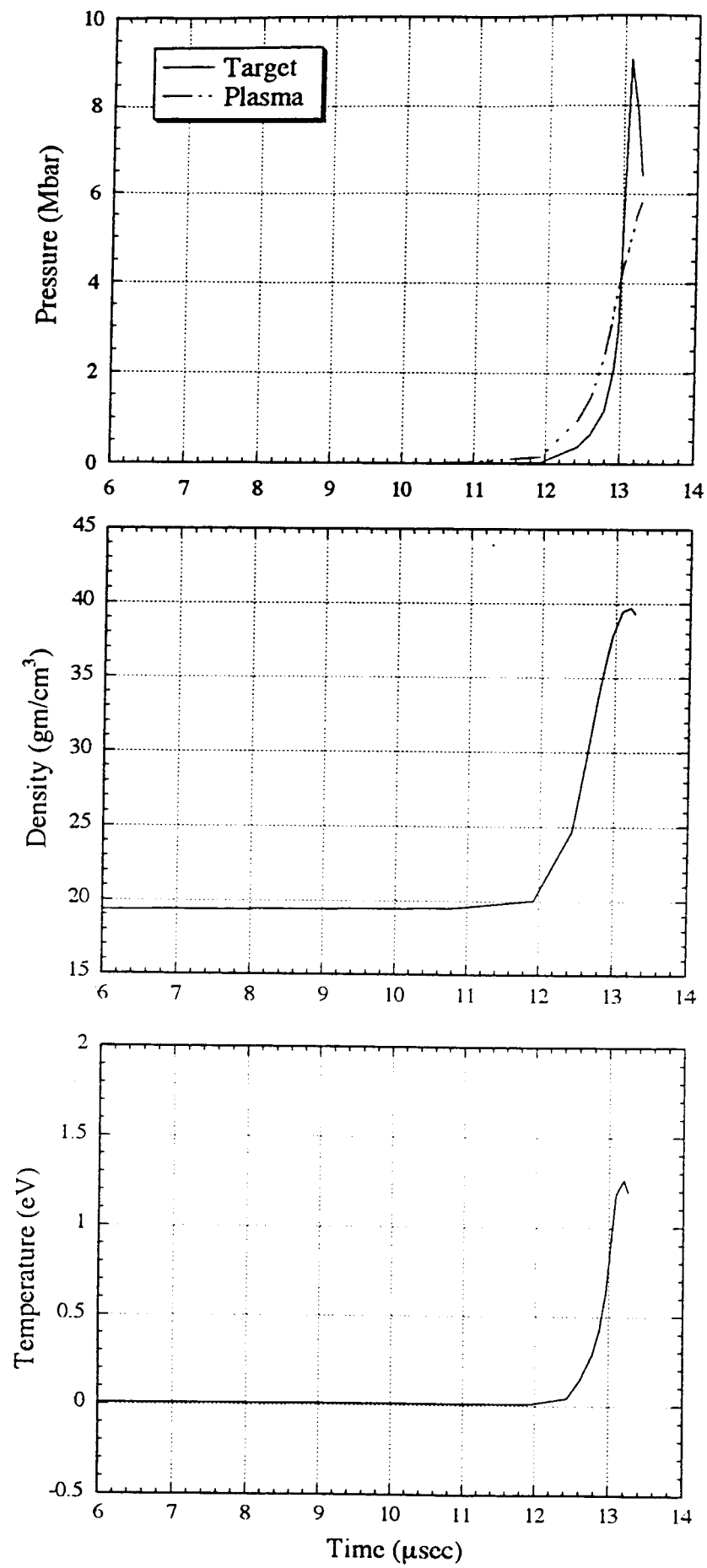


Fig. 7

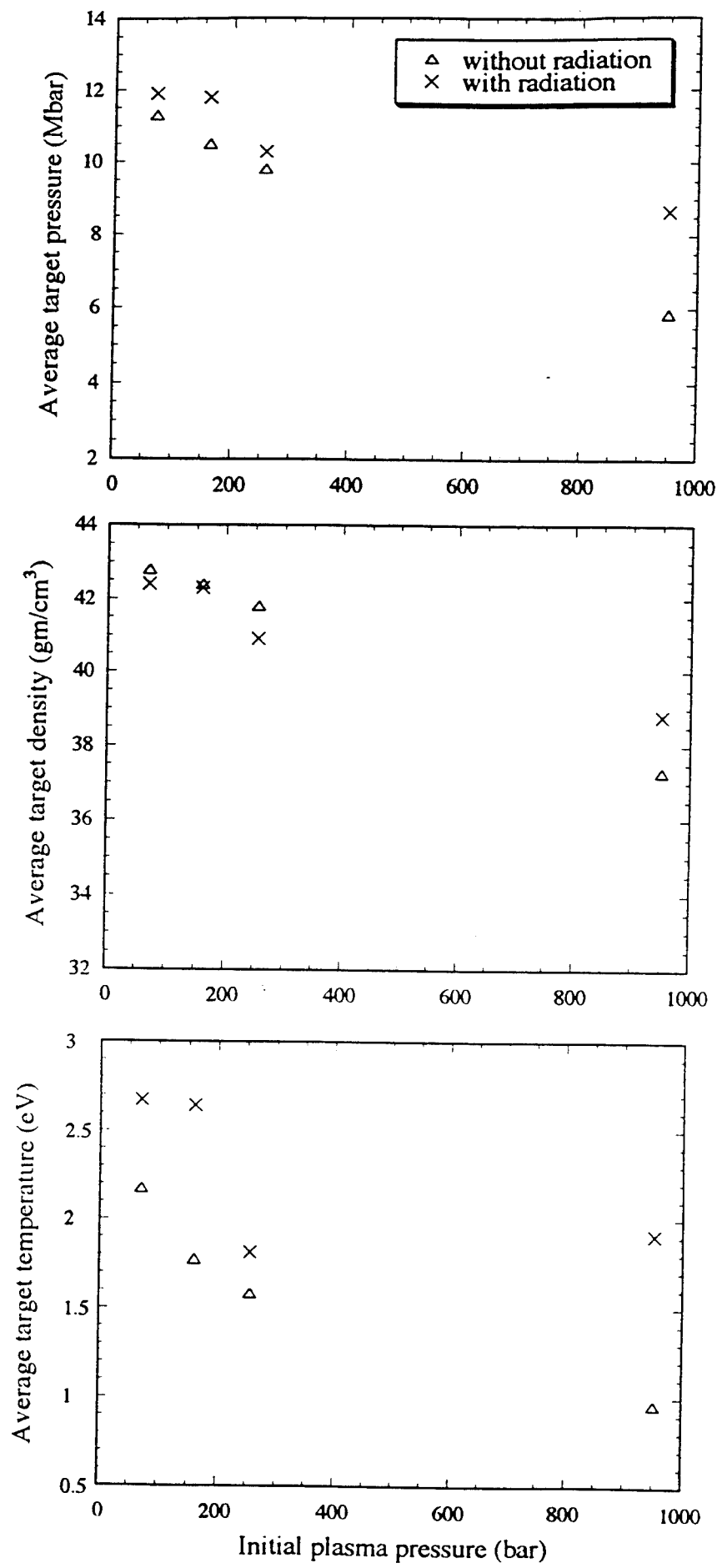


Fig. 8

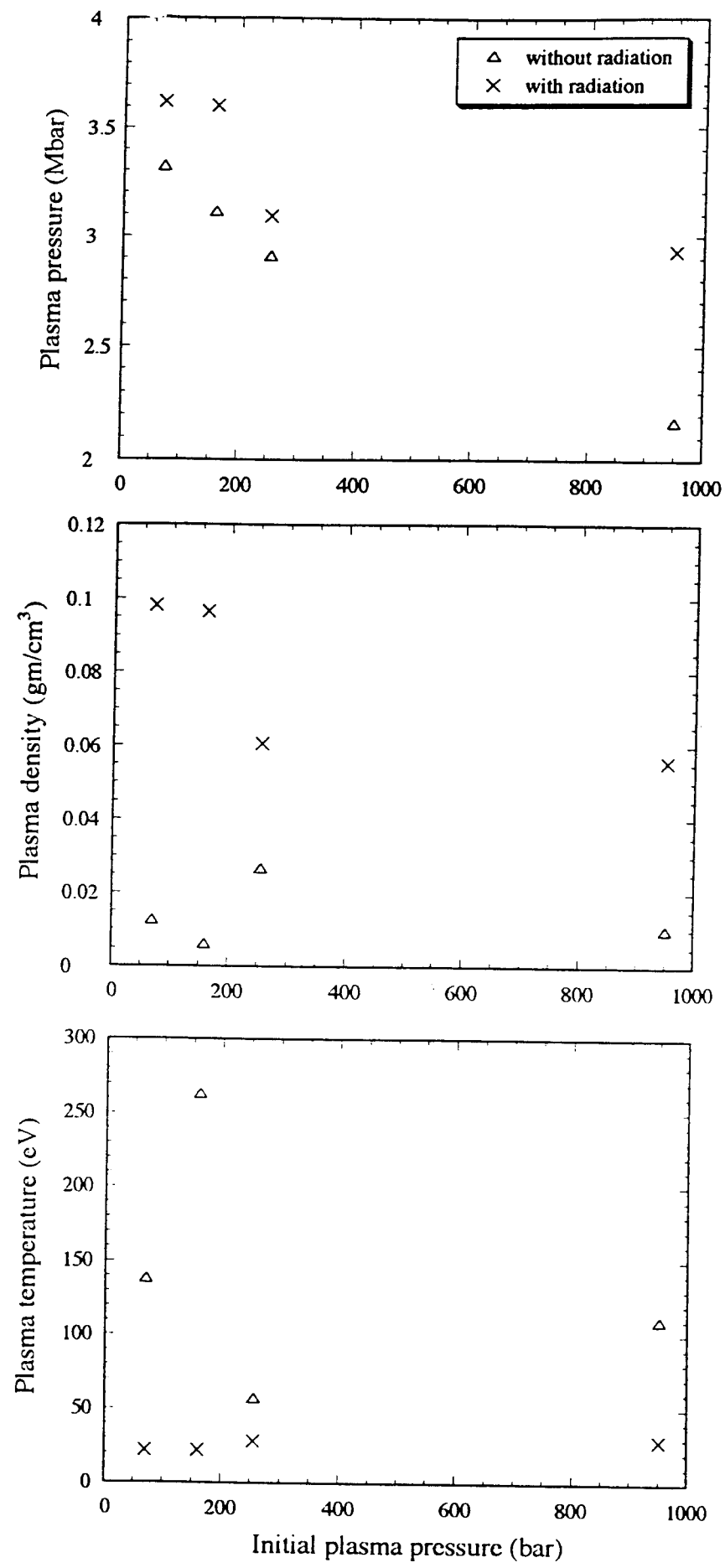


Fig. 9

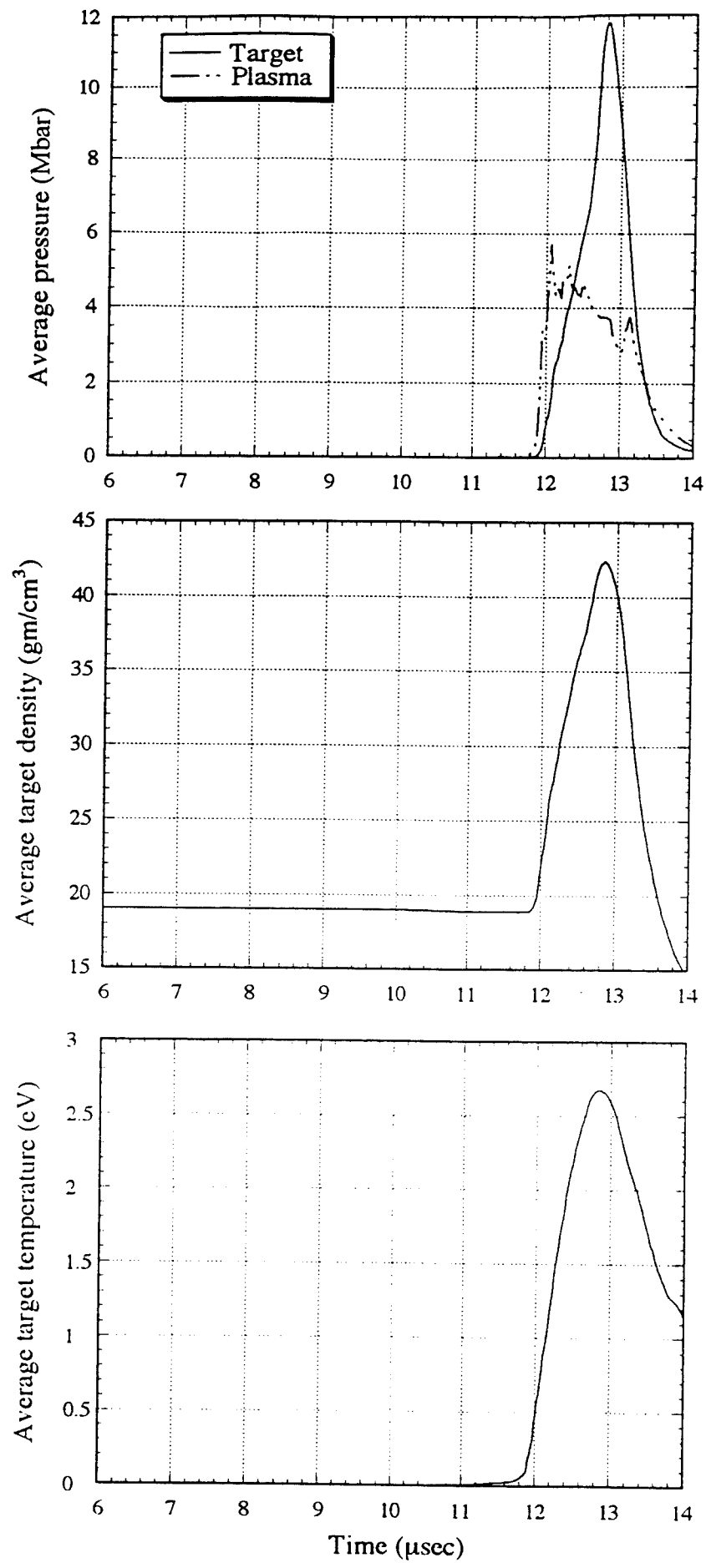


Fig. 10

APPENDIX IV

Submitted to PRL

ELECTROMAGNETIC IMPLOSION OF SPHERICAL LINER

J.H. Degnan, F.M. Lehr, J.D. Beason¹, G.P. Baca, D.E. Bell, A.L. Chesley, S.K. Coffey²,
D. Dietz, D.B. Dunlap³, S.E. Englert, T.J. Englert, D.G. Gale³, J.D. Graham³, J.J.
Havranek, C.D. Holmberg, T.W. Hussey, R.A. Lewis⁴, C.A. Outten, R.E. Peterkin, Jr.,
D.W. Price, N.F. Roderick, E.L. Ruden, U. Shumlak, G.A. Smith⁴, P.J. Turchi

High Energy Plasma Division, Phillips Laboratory, Kirtland AFB, NM

¹*US Air Force Academy, Colorado Springs, CO*

²*Physical Sciences, Inc., Alexandria, VA*

³*Maxwell Laboratories, Inc., Albuquerque, NM*

⁴*Pennsylvania State University, State College, PA*

(April 6, 1994)

Abstract

We have driven a tapered thickness spherical aluminum shell implosion with a 12.5 MA axial discharge. The initially 4 cm radius, 0.1 to 0.2 cm thick, $\pm 45^\circ$ latitude shell was imploded along conical electrodes. The implosion time was approximately 15 μ sec. Radiography indicated substantial agreement with 2D-MHD calculations. Such calculations for this experiment indicate final inner surface implosion velocity of 2.5 to 3 cm/ μ sec, peak pressure of 56 Mbar, and peak density of 16.8 gm/cm³ (>6 times solid density).

52.55.Ez, 50., 52.50.-b, 52.50.Lp

Fast solid density shell implosions, particularly in spherical geometry, may be used to obtain physical regimes of 10 to 100 Mbar pressures with 1 to 10 gm masses in the laboratory. Such regimes can be useful for studies of equation of state of materials and possibly for applications including magnetized target fusion [1]. We have previously worked on electromagnetically driven solid density shell implosions in cylindrical and conical geometry [2,3]. These experiments agreed well with two dimensional magnetohydrodynamic (2D-MHD) calculations - which predicted aluminum liner compressions to 10 Mbar, 3x solid density. We now report on such an experiment in spherical geometry.

Previous related work by others in cylindrical geometry included that by Alikhanov et al. [4], Eskov et al. [5], Petrukhin et al. [6], Chernyshev et al. [7], Turchi et al. [8], and Sherwood et al. [9]. The deformation of electromagnetically driven cylindrical shells into spheroidal shells has been discussed by Galoviznin et al. [10] and by Chernyshev, Zharinov et al. [11]. Mokhov discussed 2D-MHD calculations of a spheroidal shell liner driven hydrodynamically by a conducting medium exploded by a large current discharge [12]. His publication also showed corroborating radiography from a reduced energy scaled experiment [12]. This was an electrothermally driven spheroidal liner.

In the work reported here, we used a 12.5 MA, 4.8 MJ capacitor discharge, with current flowing in the polar direction through a spherical aluminum shell between conical electrodes, as illustrated in Figure 1. This is the first direct electromagnetically driven spherical liner implosion. The outer surface of the $\pm 45^\circ$ shell is spherical, with 4.0 cm radius. The thickness is proportional to the cosecant squared of the polar angle as measured from the symmetry axis of the electrodes (co-latitude). The thickness at the "equator" is 0.10 cm. Deviation of the actual shell thickness from the intended thickness vs. polar angle was $\lesssim 5$ percent. The mass was 49 gm. The outer surface was polished to a mirror finish. This polar angle variation of thickness causes the ratio of magnetic pressure to shell areal mass density to be independent of polar angle, assuming no polar mass flow. Ideally, this enables the spherical shape to be maintained during the implosion.

To compensate for shell-electrode contact effects, the conical electrodes are overconverged

by 3° each. That is, while the zero order design has 45° conical electrodes (whose projected vertices coincide at the origin of the electrode cylindrical co-ordinate system), the actual design has 42° (with respect to axis) conical electrodes. Their vertices project beyond the midplane from the respective electrodes. These electrodes are truncated at an axial distance of 1 cm from each other (0.5 cm from the origin).

The 1300 μ F, 120 kV, 9.4 MJ Shiva Star capacitor bank was used to drive the implosion discharge. The charge voltage and energy were 86 kV, 4.8 MJ. The initial inductance up to the outer surface of the spherical shell was 39 nH. Of this, 33 nH is in a very conservative design vacuum current feed. This vacuum current feed inductance can, in principle, be substantially reduced, enabling higher current, faster implosions. The series resistance was approximately $1 \text{ m}\Omega$ plus the resistance of a safety fuse [2,3]. This 94 cm long, 2.125 cm^2 cross section aluminum thermister/fuse limits peak discharge current and reversal in the event of an insulator or current feed failure. It has a small but non-negligible effect on a normal discharge. Its resistance during the time of interest ranges from 0.12 to $\sim 0.5 \text{ m}\Omega$. The peak discharge current, measured by integrated inductive Rogowski and azimuthal magnetic probes, is $12.5 \pm 0.5 \text{ MA}$. The current rise time is 9 μsec . The azimuthal magnetic probes indicated full current delivery in the vacuum section of the transmission line for 16 μsec into the discharge. The vacuum chamber pressure was $\sim 10^{-6} \text{ Torr}$ prior to the discharge.

The principal experimental diagnostic was pulsed radiography, taken with 300 kV, 5 kA, 30 nsec pulse driven X-ray tubes. The tubes have tungsten anodes (9.13° or 14.25° conical tips), carbon felt cathodes, and 3 mm anode-cathode coaxial gaps. They are normally damaged in such experiments, but readily refurbished. Only cylindrical radial views were used. The source to axis distance is 31.3 cm. The axis to film distance is 37.5 cm. The diagnostic X-rays pass through a 0.64 cm thick, 10 cm radius cylindrical outer current conductor, and through film pack shielding as well as through the spherical shell. The film pack shielding consists of 0.64 cm aluminum, 3.8 cm polyethylene, and 3.8 cm of low density foam. The film is DuPont NDT 57, with NDT 9 front and back screens. There were three X-ray tubes and film packs used on this experiment. Two were fired at 12.7 μsec and one

at 14 μ sec into the discharge. Collimation shielding and setup shots eliminated possible crosstalk complications. The earlier radiographs, taken with views 60° apart in azimuth, showed essentially identical images. X-ray pulser timing was confirmed using silicon PIN X-ray detectors.

Radiographs of the implosion taken at $t=0$, 12.7, and 14 μ sec into the discharge are shown in Figure 2. Also shown are 2D-MHD calculated synthetic radiographs and contours of the inner and outer liner surface. There is good agreement on the experimental and calculated shapes, locations, and timing.

The radiographs show some evidence of short (\sim mm) and long (\sim cm) wavelength non-uniformities. These do not appear to threaten the integrity of the imploding shell. These non-uniformities may be Rayleigh-Taylor instabilities of liquid and plastic portions of the liner. They will be discussed at greater length in a separate paper, for both cylindrical and spherical geometry. The 12.7 μ sec radiographs (one shown here) were taken with the sharper 9.13° anode X-ray tubes, which are higher resolution. This may be why the shorter wavelength non-uniformities are more evident than on the 14 μ sec radiograph.

The 2D-MHD calculations were done using the CALE code [13,14]. We used version 930313 of this code, with the Steinberg-Guinan elastic-plastic strength model and a 4-phase equation of state for aluminum. We ran this Arbitrary Lagrangian-Eulerian (ALE) code in Eulerian mode for \sim 1300 cycles, with 25 axial \times 75 radial zones.

The 2D-MHD calculated synthetic radiographs assume 300 keV monoenergetic X-rays and linear film response. They are contours of chordal path integrals of density times opacity. They may be a more valid comparison to the experimental radiographs than the surface or density contour plots, at least until more complete analysis of the experimental radiographs is accomplished.

There is no substantial deviation of the shape of the outer liner surface from spherical either observed or calculated until late in the implosion ($t > 12.7 \mu$ sec, $r < 2.3$ cm). The deviation from spherical shape of the outer surface that then occurs is initially consistent with an approximately incompressible liner material. The liner parameters were chosen so

that resistive heating would not cause bulk vaporization prior to the liner reaching the axis. Thus, the bulk of the liner material should be solid (albeit plastically deformed) or liquid prior to self-stagnation. If the liner were incompressible, and there were no polar mass flow, the outer surface would not implode to a radius less than 1.67 cm at the "equator", nor to a radius less than 2.1 cm at the electrode polar angle. That is, in this approximation, $r_2^3 - r_1^3 = K_o \csc^2 \phi$, where $K_o = r_{20}^3 - r_{10}^3$, and r_{20} , r_{10} are the initial outer and inner radii at the "equator".

The radius of the liner can be estimated from the circuit inductance. In a low impedance discharge such as this, L_p vs t is obtained from the experimental current I and voltage V_p vs t . V_p is the voltage measured at the (capacitive) voltage probe location, 33.9 nH from the initial liner outer surface position (cf. Figure 1). We assume that the initial voltage at this position is the inductance ratio (33.9/39) times the charge voltage (86 kV), that is, 75 kV. (L_p is initially 33.9 nH.) The resistance past the voltage probe, R_2 , is approximately 0.6 mΩ and assumed constant. This assumption may be incorrect by ~0.1 mΩ over the time of interest. L_p vs t is then obtained in the standard way:

$$L_p = \frac{1}{I} \int_0^t (V_p - IR_2) dt. \quad (1)$$

For self similar implosion geometry (i.e., electrodes not overconverged), the current radius r_c vs t is related to L_p vs t by

$$\begin{aligned} \Delta L_p &= L_p - L_{po}, \\ &= \frac{1}{I} \int B dA, \\ &= 2\left(\frac{\mu_o}{2\pi}\right) \int_{r_c}^{r_o} \int_{\phi_m}^{\pi/2} \frac{rd\phi dr}{r \sin \phi}, \\ &= \frac{\mu_o}{\pi} (r_o - r_c) \left[-\ln\left(\tan \frac{\phi_m}{2}\right)\right], \\ &= \frac{\mu_o g}{\pi} (r_o - r_c), \end{aligned} \quad (2)$$

where ϕ_m = (co-latitude) polar angle of the electrode, r_o = initial outer (spherical) current radius (presumably equal to initial outer liner radius), and μ_o = magnetic permeability =

$4\pi \times 10^{-7}$ H/m. The geometry factor $g = 0.881$ when $\phi_m = 45^\circ$. The relation is slightly more complicated for overconverged electrodes. In principle, this analysis gives the current radius vs time. In practice, the errors can be large, with uncertainty in R_2 the major source of error. A reasonable value of R_2 (0.6 m Ω) give reasonable r_c vs t . This final equation is also used to calculate the increasing load inductance (and its derivative dL/dt) in the modeling the capacitor discharge driving the implosion. In this use, the total series resistance matters, but the calculation is not sensitive to the relative portion of the total resistance past the voltage probe. A comparison of the experimental (spherical) current radius vs time with the 2D-MHD calculated inner and outer liner (spherical) radius vs time t is shown in Figure 3. Since the shape deviates from spherical once the incompressible limiting radius at the electrode polar angle is reached, the calculated r vs t is shown for a given polar angle ($\phi=90^\circ$ =equator). The more reliable radiography data points are also shown on this plot.

The degree of agreement between experimental and 2D-MHD calculated results encourages us to extend the 2D-MHD predictions through peak compression. Some principal results for a calculation for this experiment are shown in Figure 4. These indicate that a large portion of the liner mass is compressed to greater than twice solid density and on the order of a gram is compressed to ~ 6 x solid density, 56 Mbar. The predicted inner surface implosion velocity reaches 2.5 to 3 cm/ μ sec at a radius of 0.2 cm. The predicted peak implosion kinetic energy is ~ 1 MJ.

Similar calculations with less conservative electrodes (not overconverged) indicate more distortion of the liner near the electrode, but not enough to cause liner-electrode detachment. Such calculations indicate higher peak compressions, ~ 90 Mbar.

This research was supported by the Air Force Office of Scientific Research. We would like to acknowledge the support and interest of Drs W.L. Baker, B. Godfrey, R. Kelley, G. Kiutu, and H. Wittmann.

REFERENCES

- [1] I. Lindemuth and R. Kirkpatrick, *Nuclear Fusion* **23**, 263 (1983).
- [2] J. Degnan *et al.*, in *Megagauss Technology and Pulsed Power Applications*, Fourth International Conference on Megagauss Magnetic Field Generation and Related Topics, edited by C. Fowler, R. Caird, and D. Erickson (Plenum Press, New York, NY, 1987), pp. 699-706.
- [3] J. Degnan *et al.*, in *Megagauss Fields and Pulsed Power Systems*, Fifth International Conference on Megagauss Magnetic Field Generation and Related Topics, edited by V. Titov and G. Shvetsov (Nova Science Publishers, Inc., New York, NY, 1990), pp. 623-630.
- [4] S. Alikhanov, V. Bakhtin, and D. Toporkov, in *Ultrahigh Magnetic Fields - Physics, Techniques, Applications*, Third International Conference on Megagauss Magnetic Field Generation and Related Topics, edited by V. Titov and G. Shvetsov (Nauka, Moscow, 1984), p. 213.
- [5] A. Eskov, M. Kitayev, and R. Kurtmullayev, in *Ultrahigh Magnetic Fields - Physics, Techniques, Applications*, Third International Conference on Megagauss Magnetic Field Generation and Related Topics, edited by V. Titov and G. Shvetsov (Nauka, Moscow, 1984), p. 204. See Ref. [4].
- [6] A. Petrukhin *et al.*, in *Ultrahigh Magnetic Fields - Physics, Techniques, Applications*, Third International Conference on Megagauss Magnetic Field Generation and Related Topics, edited by V. Titov and G. Shvetsov (Nauka, Moscow, 1984), p. 406. See Ref. [4].
- [7] V. Chernyshev *et al.*, in *Megagauss Technology and Pulsed Power Applications*, Fourth International Conference on Megagauss Magnetic Field Generation and Related Topics, edited by C. Fowler, R. Caird, and D. Erickson (Plenum Press, New York, NY, 1987),

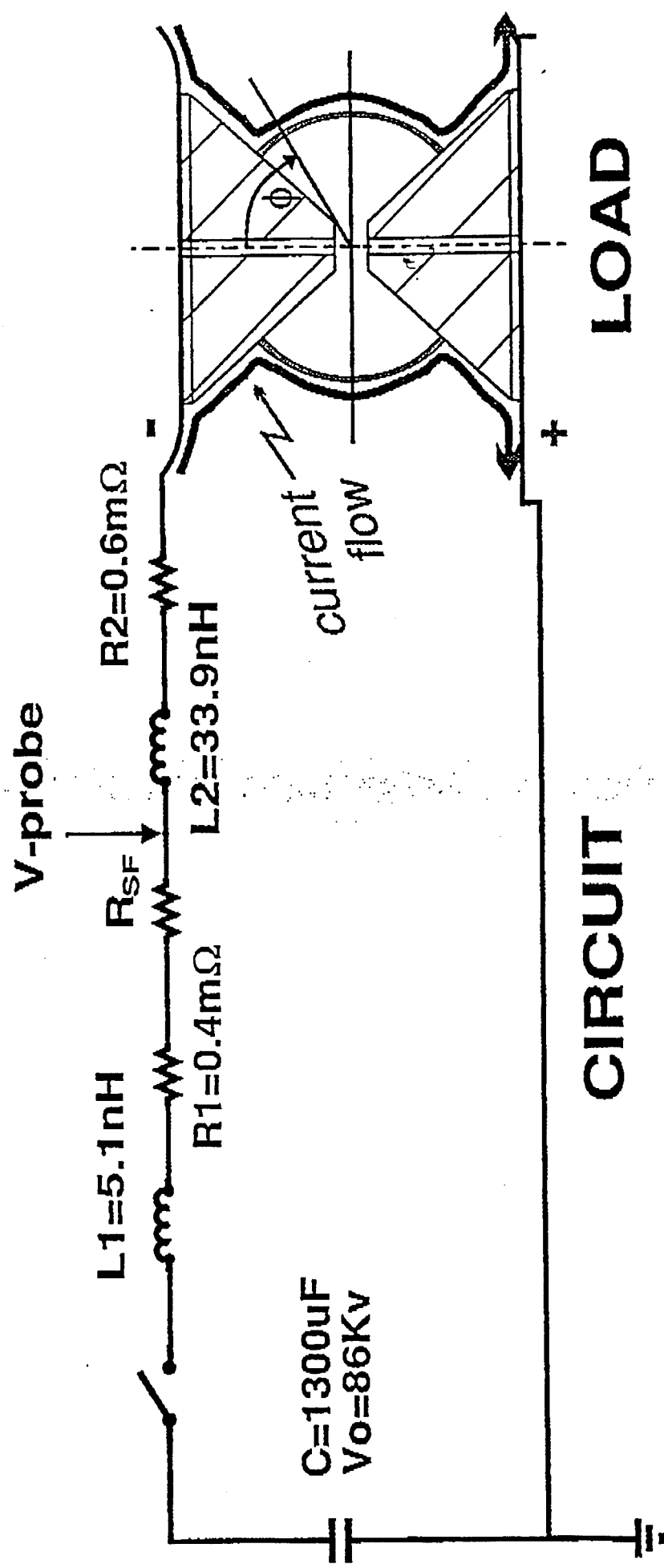
pp. 707-712. See Ref. [2].

- [8] P. Turchi *et al.*, in *Megagauss Physics and Technology*, Second International Conference on Megagauss Magnetic Field Generation and Related Topics, edited by P. Turchi (Plenum Press, New York, NY, 1980), p. 375.
- [9] A. Sherwood *et al.*, in *Megagauss Physics and Technology*, Second International Conference on Megagauss Magnetic Field Generation and Related Topics, edited by P. Turchi (Plenum Press, New York, NY, 1980), pp. 391-398. See Ref. [8].
- [10] V. Goloviznin *et al.*, in *Megagauss Physics and Technology*, Second International Conference on Megagauss Magnetic Field Generation and Related Topics, edited by P. Turchi (Plenum Press, New York, NY, 1980), p. 415. See Ref. [8].
- [11] V. Chernyshev *et al.*, in *Sixth International Conference on Megagauss Magnetic Field Generation and Related Topics*, Sixth International Conference on Megagauss Magnetic Field Generation and Related Topics, edited by M. Cowan and R. Spielman (Nova Science Publishers Inc., Commack, NY 11725, in press).
- [12] V. Mokhov *et al.*, Sov. Phys. Dokl. 24, 557 (1979).
- [13] R. Tipton, in *Megagauss Technology and Pulsed Power Applications*, Fourth International Conference on Megagauss Magnetic Field Generation and Related Topics, edited by C. Fowler, R. Caird, and D. Erickson (Plenum Press, New York, NY, 1987), p. 299. See Ref. [2].
- [14] R. Tipton, *CALE Users Manual* (Lawrence Livermore National Laboratory, Livermore, CA, 1990).

FIGURES

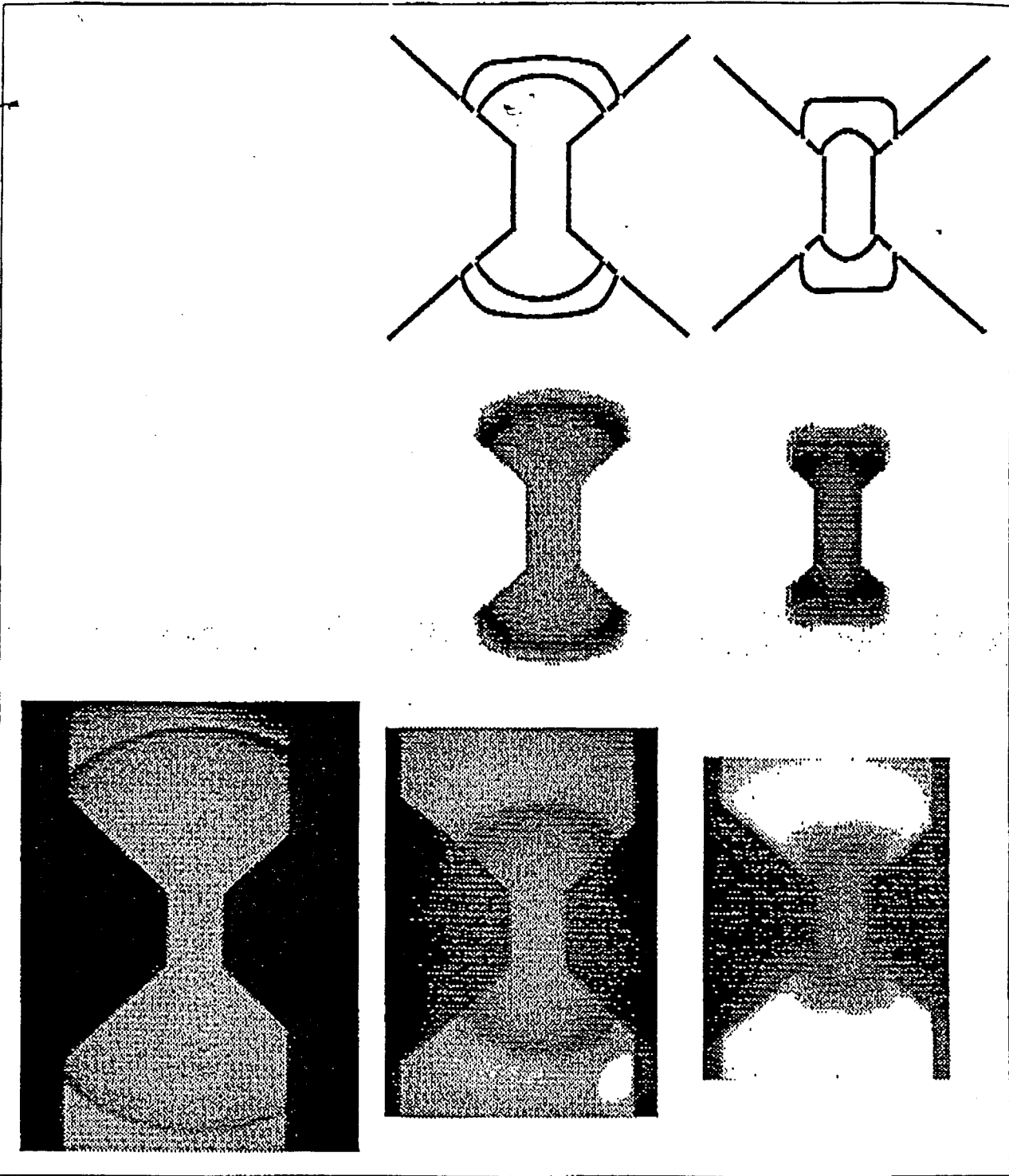
FIG. 1. Circuit Diagram & Load Schematic

FIG. 2. Radiographs (at $t_1, t_2, t_3 = 0, 12.7, 14 \mu\text{sec}$), 2D-MHD (at $t_2, t_3 = 12.7, 14 \mu\text{sec}$) ComparisonFIG. 3. Calculated, Experimental r vs. t FIG. 4. Calculated density (ρ) vs. r at $z=0$ for 12.7, 14.0, 15.0 μsec . Calculated pressure (p) vs. r at $z=0$ for peak compression (15.0 μsec)



Radiographs

Experimental Synthetic
Surface
Contours



t_1

t_2

t_3

